HEALTH AND MEDICINE

Ω76: A designed antimicrobial peptide to combat carbapenem- and tigecycline-resistant *Acinetobacter baumannii*

Deepesh Nagarajan[1], Natasha Roy[2], Omkar Kulkarni[1], Neha Nanajkar[1], Akshay Datey[3], Sathyabaarathi Ravichandran[1], Chandrani Thakur[1], Sandeep T.[4], Indumathi V. Aprameya[4], Siddhartha P. Sarma[2,5], Dipshikha Chakravortty[3]*, Nagasuma Chandra[1]*

Drug resistance is a public health concern that threatens to undermine decades of medical progress. ESKAPE pathogens cause most nosocomial infections, and are frequently resistant to carbapenem antibiotics, usually leaving tigecycline and colistin as the last treatment options. However, increasing tigecycline resistance and colistin's nephrotoxicity severely restrict use of these antibiotics. We have designed antimicrobial peptides using a maximum common subgraph approach. Our best peptide (Ω76) displayed high efficacy against carbapenem and tigecycline-resistant *Acinetobacter baumannii* in mice. Mice treated with repeated sublethal doses of Ω76 displayed no signs of chronic toxicity. Sublethal Ω76 doses co-administered alongside sublethal colistin doses displayed no additive toxicity. These results indicate that Ω76 can potentially supplement or replace colistin, especially where nephrotoxicity is a concern. To our knowledge, no other existing antibiotics occupy this clinical niche. Mechanistically, Ω76 adopts an α-helical structure in membranes, causing rapid membrane disruption, leakage, and bacterial death.

INTRODUCTION

The emergence of drug-resistant pathogens has proven to be a grave public health problem. Worldwide, 5.3 million deaths occur annually due to antibiotic-resistant infections (*1*). This number can be expected to increase over time (*2*), especially for patients admitted to intensive care units (ICUs). Globally, a third of all ICU patients develop drug-resistant infections (*3*), which substantially increase patient mortality and health care costs (*4*–*6*). The multidrug-resistant ESKAPE pathogens, namely, *Enterococcus faecium*, *Staphylococcus aureus*, *Klebsiella pneumoniae*, *Acinetobacter baumannii*, *Pseudomonas aeruginosa*, and *Enterobacter* spp., have emerged as the leading causes of nosocomial infections. The emergence of pathogenic *A. baumannii* is particularly problematic and has been aided by two factors (*7*): its remarkable ability to uptake genetic material encoding drug resistance from the environment and its ability to survive in a hospital environment for prolonged time periods. For these reasons, *A. baumannii* has received a Priority-1 (critical) classification by the World Health Organization for the development of new antibiotics (*8*).

Carbapenem class antibiotics are drugs of last resort for multidrug-resistant bacterial infections. However, resistance to carbapenems is now widespread (*9*), ranging from 46 to 66% across different countries (*10*, *11*). In *A. baumannii*, carbapenem resistance is caused by metallo-β-lactamases, carbapenem-hydrolyzing oxacillinases, and modified penicillin-binding proteins (*12*). In cases of carbapenem resistance, treatment options are usually limited to the antibiotics tigecycline and colistin (*13*). Unfortunately, tigecycline resistance is also rapidly increasing. One study reported tigecycline resistance in 66% of all *A. baumannii* isolates collected (*14*). In *A. baumannii*, multidrug efflux pumps are responsible for tigecycline resistance (*15*). In these cases, colistin remains the only treatment option. However, approximately half of all patients treated with colistin develop acute kidney injury (*16*–*18*). Because of these limited treatment options, there is a pressing need for new antibiotics to combat *A. baumannii* specifically and ESKAPE pathogens in general.

Antimicrobial peptides (AMPs) are ancient components of the innate immune system found across all kingdoms of life (*19*) and are promising candidates for the development of new drugs. Their primary mechanism of action involves incorporation into bacterial membranes through coulombic attraction, followed by membrane disruption, cytoplasmic leakage, and bacterial death. By targeting an entire cellular component rather than a specific molecule, AMPs evade the development of resistance mechanisms for single-target drugs such as carbapenems and tigecycline. Three detailed mechanisms describing AMP incorporation and disruption have been proposed: toroidal pore formation (*20*), barrel stave formation (*21*), and carpet formation (*22*). AMPs also have secondary mechanisms of action such as metabolic inhibition (*23*, *24*); inhibition of DNA (*25*), RNA (*26*), and protein synthesis (*27*, *28*); inhibition of translation termination (*29*); inhibition of septum formation (*30*); inhibition of cell wall synthesis (*31*); induction of ribosomal aggregation (*32*); and delocalization of membrane proteins (*33*).

For two decades, peptide designers have attempted to improve the properties of AMPs through intuitive in cerebro and in silico approaches, both of which have yielded multiple successes. In cerebro designs typically involve increasing the positive charge, helicity, or hydrophobicity of natural AMPs or involve the de novo design of simple repeating motifs. Pexiganan (*34*), a lysine-rich magainin analog, is one such example of an early in cerebro design. SAAP-148 (*35*), created by improving the cationicity and helicity of LL-37, is a contemporary example. Other peptides with tryptophan-arginine repeat motifs (*36*), leucine-lysine repeat motifs (*37*, *38*), tryptophan-leucine-lysine repeat motifs (*39*), and lysine-valine disordered repeats as part of nanoengineered materials (*40*) have all displayed promising antimicrobial activity. Later in silico

[1]Department of Biochemistry, Indian Institute of Science, Bangalore 560012, India. [2]Molecular Biophysics Unit (MBU), Indian Institute of Science, Bangalore 560012, India. [3]Department of Microbiology and Cell Biology, Indian Institute of Science, Bangalore 560012, India. [4]Department of Microbiology, M.S. Ramaiah Medical College, Bangalore 560054, India. [5]NMR Research Center, Indian Institute of Science, Bangalore 560012, Karnataka, India.
*Corresponding author. Email: nchandra@iisc.ac.in (N.C.); dipa@iisc.ac.in (D.C.)

approaches have relied heavily on machine learning and optimization algorithms. Peptides designed using quantitative structure–activity relationship (QSAR) models (*41*), linguistic models (*42*), deep-learning long short-term memory (LSTM) models (*43*), and genetic algorithms (*44*, *45*) have all seen varying degrees of success. Despite these successes, AMPs have not yet been approved for clinical use. Systemic toxicity is a primary drawback (*46*–*48*), which restricts the use of many AMPs to topical treatment.

This work casts AMP design as a computational graph optimization problem. A database of existing α-helical AMP structures has been reduced to a graphical representation. Amino acid residues are represented as nodes, and covalent/hydrogen bonds are represented as edges. We generated new graphs by optimizing the superposition of existing subgraphical motifs such that the largest number of database subgraphs was represented within our new design. This approach was used to design and experimentally characterize five peptides. Our best peptide (Ω76) displayed in vitro and in vivo efficacy against carbapenem- and tigecycline-resistant organisms and negligible in vivo toxicity at sublethal doses. Further, time-kill curves, phosphate leakage radioassays, confocal microscopy, scanning electron microscopy (SEM), microarray gene expression experiments, and nuclear magnetic resonance (NMR) spectroscopy all helped understand the mechanism of action of Ω76.

RESULTS

Here, we describe the computational design of Ω-family peptides using a maximum common subgraph approach. We describe the in vitro characterization of our peptides against type cultures and drug-resistant clinical isolates. We describe in vitro toxicity assays performed using human blood and cell lines, followed by in vivo toxicity assays performed on BALB/c mice. We describe in vivo efficacy experiments performed for peptide Ω76 against carbapenem- and tigecycline-resistant *A. baumannii*, using a BALB/c mouse model of peritoneal infection. Last, we describe multiple experiments to understand the mechanisms of action of Ω76.

Maximum common subgraphs and their utilization for AMP design

Three-dimensional (3D) structures of α-helical AMPs can be reduced to graphical representations. Individual amino acid residues can be reduced to nodes. For the 20 canonical amino acids, 20 different node types exist. Similarly, inter-residue interactions can be reduced to edges. Inter-residue backbone covalent bonds (N→C) were modeled as directed edges. Similarly, inter-residue backbone hydrogen bonds (N─H→C═O) were modeled as directed edges. Therefore, any given node must contain a minimum of one edge (N→C or C→N edge) and a maximum of four edges (N→C, C→N, N─H→C═O, and C═O→N─H). Further, each node can have a maximum of one type of edge (for example, it is impossible for a single node to have two C→N edges).

A dataset containing 74 α-helical structures of known AMPs extracted from the Antimicrobial Peptide Database (APD) (*49*) was reduced to such a graphical representation. A small dataset of AMP structures, rather than a large dataset of AMP sequences, was chosen for this study as structures are more data rich. Important subgraphical information would be absent in sequences alone. Using this dataset, we attempted to generate AMPs through maximum common subgraph matching. Our approach can be explained using a 1D analogy: Consider AMPs ABCDE and BCDEFG. A superposition of their common sequences would yield peptide ABCDEFG, where BCDE is analogous to the maximum common subgraph shared between the two peptides. Biologically, these subgraphs would be representations of AMP motifs. Because AMPs are subject to selection pressures, a motif would occur frequently only if it bestowed its parent peptide with greater antimicrobial efficacy. We anticipated that designing peptides using an energy function that encouraged the largest possible number of superposed subgraphs would therefore display enhanced antimicrobial activity.

Designing AMPs sharing the largest number of maximum common subgraphs with the 74-member peptide database was performed using simulated annealing optimization. Simulated annealing is an efficient approach for finding a good approximation of the global minimum of any energy function and is extensively used for protein design (*50*–*52*). Starting with a 20-residue blank peptide template, at each iteration of the simulated annealing protocol, a residue was randomly selected and mutated. The entire template was then scanned across the peptide database to detect any subgraph matches. The template was scored on the basis of the total number of matching nodes in the peptide database. Mutations improving this score were unconditionally accepted. Mutations decreasing this score were probabilistically accepted or rejected depending on the global state of the simulated annealing protocol. Two thousand iterations were performed to exhaustively sample graph space, with each residue being mutated 100 times on average. To avoid generating homopolymeric peptides, a subgraph was defined to have a minimum of five residues per node. For clarity, a single iteration of the simulated annealing protocol is illustrated in Fig. 1.

The unique properties of α-helical graphs reduce subgraph isomorphism detection from a nondeterministic polynomial-time (NP) complete, exponential computational problem to a polynomial problem with $\mathbf{O}(m \times n^3)$ complexity, where n is the average number of residues for AMPs and m is the number of database AMPs (here, 74).

The algorithm and peptide database described here have been incorporated into the Heligrapher software package. The Heligrapher database, Python source code, and usage examples have been stored on the GitHub repository (https://github.com/1337deepesh/Heligrapher) and are also provided in protocol S1. Heligrapher was used to design 1000 α-helical AMP graphs. The top 5 scoring graphical representations were converted into sequences (named Ω03→Ω93) and synthesized for this study (Table 1). All peptides appeared lysine rich and amphiphilic. The

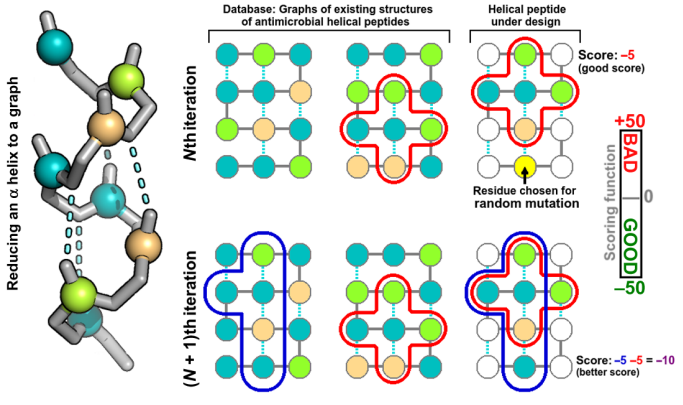

Fig. 1. An illustration of a single step of AMP design using Heligrapher, showing how the maximum common subgraph scoring scheme functions.

common subgraphical motifs shared between all peptides are described in fig. S1 and table S1.

To validate the algorithm described here, the Heligrapher energy function was inverted and used to design poor-scoring shuffled variants of Ω76 (Ω76-shuf1→4; Table 1) containing no common subgraphs. Despite having the same amino acid composition of 76, we hypothesized that these peptides would display poor antimicrobial activity as they would share no evolutionarily conserved graphical motifs with natural AMPs. The experimental characterization of these peptides is described in the "In vitro efficacy of Ω17 and Ω76 against drug-resistant clinical isolates" section.

In vitro efficacy of designed AMPs against type cultures

We synthesized and experimentally characterized five peptides designed using the Heligrapher software package (Table 1). Initially, we tested these peptides against a diverse panel of pathogens of Gram-positive, Gram-negative, fungal, and mycobacterial origin. A peptide concentration range of 0.25 to 128 mg/liter was used for minimum inhibitory concentration (MIC) assays. Five peptides assayed against 30 organisms resulted in 150 MIC values provided in table S2.

Designed peptides were ranked on the basis of a previously described relative scoring scheme (I_score) (*43*). This score was based on the number of bacterial cultures a peptide inhibited with the lowest MIC, as compared to the MICs of all other designed peptides for that given culture (Eq. 1).

$$\text{I\_score}_j = \sum_{i=1}^{M} \mathbb{I}\left\{X_{ij} = \min_{j=1}^{N}(X_i)\right\} \text{where} : 0 \le i \le M, 0 \le j \le N \quad (1)$$

Here, X represents a matrix of MIC values. M represents rows that contain MIC values for a given organism. N represents columns that contain MIC values belonging to a given peptide. Note that multiple minimum MIC values can occur for any given row. Using Eq. 1, the two best performing peptides were identified to be Ω17 (I_score = 19) and Ω76 (I_score = 6). These peptides were therefore chosen for further characterization.

Table 1. The Ω-family peptides. (Top) Names, sequences, and I_scores of all Ω-family peptides synthesized for this study. Note that pexiganan was used as a toxicity control. (Bottom) Sequence alignment between Ω76 and pexiganan. Despite some similarities, the two peptides display vastly different toxicological profiles, as described in the "In vitro and in vivo toxicity of designed AMPs" section.

Peptide	Sequence	I_score
Ω03	KLGKKLRKKLKKIGKGLKAI	3
Ω13	KAIKRIGKRIKKLLLKLKKK	5
Ω17	RKKAIKLVKKLVKKLKKALK	19
Ω76	FLKAIKKFGKEFKKIGAKLK	6
Ω93	IKALGKKLRKGKKKIGKKVK	1
Pexiganan	GIGKFLKKAKKFGKAFVKILKK	Not tested
Ω76-shuf1	AFLLKKKKGIIFFEKAKKGK	Not tested
Ω76-shuf2	AKKKKFIFIKEKAFLLKGKG	Not tested
Ω76-shuf3	KKKKGFILILKEAFAFKKGK	Not tested
Ω76-shuf4	AKFKKEKILLFAKGKFIKGK	Not tested
Ω76	----FLKAIKKFGKEFKKIGAKLK	
Pexiganan	GIGKFLKKAKKFGKAFVKILKK--	

In vitro efficacy of Ω17 and Ω76 against drug-resistant clinical isolates

The minimum bactericidal concentrations (MBCs) of peptides Ω17 and Ω76 were assayed against a panel of 64 recent clinical isolates acquired from M.S. Ramaiah Medical College, Bangalore (tables S3 and S4) (*43*). Many of these isolates (*A. baumannii*, *K. pneumoniae*, *P. aeruginosa*, and *S. aureus*) belonged to the ESKAPE pathogen family. *Escherichia coli* and coagulase-negative Staphylococci (CoNS) were also represented. Most of these isolates displayed multidrug resistance (extended-spectrum beta lactamase, methicillin, carbapenem, and tigecycline resistance).

Ω17 appears to be slightly more effective against Gram-negative organisms (MBC_{50} = 4 mg/liter) than against Gram-positive organisms (MBC_{50} = 16 mg/liter) (Table 2, top). Ω76 was found to be effective against Gram-negative organisms only (MBC_{50} = 16 mg/liter) (Table 2, bottom). Of the Gram-positive organisms tested, only CoNS displayed some inhibition when treated with Ω76 (MBC_{50} = 32 mg/liter). However, Ω76 appeared to be nearly as effective against *E. coli* and *A. baumannii* isolates as compared to Ω17. Ω76 displayed an MBC_{50} of 4 mg/liter for both *E. coli* and *A. baumannii*, which was only twofold higher than the Ω17 MBC_{50} of 2 mg/liter for both.

Drug-resistant clinical isolates were also used to validate the Heligrapher algorithm. Four shuffled variants of Ω76 (Ω76-shuf1→4; Table 1) were designed with an inverted energy function as described in the "Maximum common subgraphs and their utilization for AMP design" section. Because of the complete absence of shared subgraphical motifs with known AMPs, Ω76-shuf1→4 were expected to have poor activity. When tested against all clinical isolates of *A. baumannii*, Ω76-shuf1→4 displayed MBC values significantly higher than Ω76 (table S5), thereby validating our computational approach.

In vitro and in vivo toxicity of designed AMPs

Briefly, HeLa cells, HaCaT cells, and human red blood cells (RBCs) were used to assay the in vitro toxicity for Ω17 and Ω76. Survival experiments, histopathology, and blood tests were used to assay the in vivo toxicity of Ω76.

In vitro cytotoxicity experiments using the HeLa and HaCaT cell lines were performed for both Ω17 and Ω76 (Fig. 2, A and B). For both peptides, the IC_{50} (half maximal inhibitory concentration) against HeLa cells was >128 mg/liter. Ω76 displayed no noticeable cytotoxicity against HeLa cells even at the highest concentration tested (mean HeLa inhibition at 128 mg/liter, Ω76 = 5.9%), whereas Ω17 displayed considerable HeLa inhibition under the same conditions (mean HeLa inhibition at 128 mg/liter, Ω17 = 36.7%). Both peptides displayed negligible toxicity when tested on the HaCaT cell line.

In vitro hemolysis experiments were performed using human blood (Fig. 2C). In both cases, the HB_{50} (peptide concentration for 50% hemolysis) value for both peptides was >128 mg/liter. Once again, Ω76 displayed no substantial hemolysis at all concentrations tested (mean hemolysis at 128 mg/liter, Ω76 = 1.78%). However, Ω17

Table 2. MBC values for Ω17 and Ω76 against clinical isolates. (Top) MBC values for Ω17 against clinical isolates. This table depicts a frequency distribution. Taking *E. coli* as an example, Ω17 inhibits six isolates with an MBC of 1 mg/liter, seven isolates with an MBC of 2 mg/liter, three isolates with an MBC of 4 mg/liter, and three more isolates with an MBC of 8 mg/liter. Therefore, the median MBC value (MBC_{50}) for *E. coli* is 2 mg/liter. (Bottom) MBC values for Ω76 against clinical isolates. Resistance phenotypes are also mentioned. CRE, carbapenem-resistant Enterobacteriaceae; ESBL, extended-spectrum beta lactamase producers; MRSA, methicillin-resistant *S. aureus*; MRCN, methicillin-resistant coagulase-negative Staphylococci.

Ω17: Organism	**Resistance**	**0.25**	**0.5**	**1**	**2**	**4**	**8**	**16**	**32**	**64**	**128**	**>128**	**MBC_{50}**
E. coli	CRE			2	2	2	3						
E. coli	ESBL			4	4	1							
E. coli					1								
Total				6	7	3	3						2
A. baumannii	CRE			1		1	1						
A. baumannii					1								
Total				1	1	1	1						2
K. pneumoniae	CRE				1		1	1		1	1		
K. pneumoniae	ESBL					1						2	
K. pneumoniae												1	
Total					1	1	1	1		1	1	3	64
P. aeruginosa	CRE						1	2				1	
P. aeruginosa	ESBL				1								
P. aeruginosa					2								
Total					3		1	2				1	8
E. faecalis							2					3	>128
CoNS	MRCN				1	3							
CoNS				1	1	1		1					
Total				1	2	4		1					4
S. aureus	MRSA				1					1		1	
S. aureus									1		3	2	
Total					1				1	1	3	3	128
Gram −ve				7	12	5	6	3		1	1	4	4
Gram +ve				1	3	4	2	1	1	1	3	6	16
Total				8	15	9	8	4	1	2	4	10	4

Ω76: Organism	**Resistance**	**0.25**	**0.5**	**1**	**2**	**4**	**8**	**16**	**32**	**64**	**128**	**>128**	**MBC_{50}**
E. coli	CRE				2	3		1	3				
E. coli	ESBL			5	2		1	1					
E. coli							1						
Total				5	4	3	2	2	3				4
A. baumannii	CRE				1	4	1						
A. baumannii						1							
Total					1	5	1						4

continued on next page

Ω76: Organism	Resistance	0.25	0.5	1	2	4	8	16	32	64	128	>128	MBC_{50}
K. pneumoniae	CRE					1	2				1	1	
K. pneumoniae	ESBL							1			1	1	
K. pneumoniae											1		
Total						1	2	1			3	2	128
P. aeruginosa	CRE						1			3			
P. aeruginosa	ESBL						1						
P. aeruginosa						1		1					
Total						1	2	1		3			16
E. faecalis									1	1		3	>128
CoNS	MRCN						1	2	2	1			
CoNS							1		2	1			
Total							1	1	4	2			32
S. aureus	MRSA							1				2	
S. aureus												6	
Total								1				8	>128
Gram −ve				5	5	10	7	4	3	3	3	2	8
Gram +ve							1	2	5	3		11	>128
Total				5	5	10	8	6	8	6	3	13	16

displayed considerable hemolysis at higher concentrations (mean hemolysis at 128 mg/liter, Ω17 = 13.91%).

Because of considerable cytotoxic and hemolytic effects, Ω17 was excluded from further in vivo toxicity experiments. However, Ω17 may still find applications as a topical agent due to its strong, broad-spectrum activity.

We determined the in vivo LD_{50} (median lethal dose) values for Ω76, colistin, and pexiganan using BALB/c mice, using a twofold concentration gradient. All compounds were injected intraperitoneally, and mice were monitored for 5 days. LD_{50} values for Ω76 (150 mg/kg), colistin (30 mg/kg), and pexiganan (60 mg/kg) were estimated by linear interpolation (Fig. 2D). The maximum sublethal doses for Ω76 (64 mg/kg), colistin (16 mg/kg), and pexiganan (32 mg/kg) were noted for use in further experiments. Ω76 appeared to be the least toxic compound tested, being 2.5× less toxic than pexiganan and 5× less toxic than colistin.

Further, we performed cumulative toxicity determination experiments for Ω76, colistin, and pexiganan (Fig. 2E). In clinical settings, antibiotic treatment courses span days to weeks and may result in toxic effects that single-dose experiments fail to capture. We intraperitoneally injected 11 maximum sublethal doses of Ω76, colistin, and pexiganan in three separate cohorts. These doses were administered over 5 days at 12-hour intervals. Ten of 10 mice treated with Ω76 survived the experiment. In comparison, only 5 of 10 mice treated with colistin and 0 of 10 mice treated with pexiganan survived the experiment. Fisher's exact test confirmed that the survival differences between the Ω76-colistin ($P = 0.032$) and Ω76-pexiganan ($P = 10^{-5}$) cohorts were statistically significant. These results indicate that Ω76 has superior acute and cumulative toxicity characteristics in comparison to an experimental therapeutic (pexiganan) and a clinical antibiotic (colistin).

Next, we investigated multidose cumulative toxicity for Ω76 by changing the time interval between doses (Fig. 2F). Three cohorts of five mice each were used. The first cohort was injected with three maximum sublethal Ω76 doses (64 mg/kg) spaced 2 hours apart. The second cohort was injected with four maximum sublethal Ω76 doses (64 mg/kg) spaced 1.5 hours apart. The third cohort was injected with five maximum sublethal Ω76 doses (64 mg/kg) spaced 1 hour apart. All mice survived for 5 days in all cohorts. These results indicate that multiple (maximum sublethal) doses of Ω76 can be administered at very short time intervals without the risk of cumulative toxicity.

We investigated whether maximum sublethal doses of colistin and Ω76 could be safely coadministered. Ten mice were injected with a combined dose of colistin (16 mg/kg) and Ω76 (64 mg/kg) and monitored for 5 days, and no mortality was observed (Fig. 2F, highlighted). In contrast, a colistin dose of 32 mg/kg caused mortality in 3 of 5 mice, and a Ω76 dose of 128 mg/kg caused mortality in 2 of 5 mice (5 of 10 mice total) (Fig. 2D, highlighted). Therefore, a combined maximum sublethal dose of colistin and Ω76 is less toxic than the minimum lethal doses of colistin and Ω76 considered separately ($P = 0.032$, Fisher's exact test). This indicates that Ω76 can be safely coadministered with colistin, without the concern of additive toxicity. Further, Ω76 and colistin do not negatively interact with each other. A checkerboard assay revealed a median ∑FIC of 0.5625, indicating a combined additive effect (fig. S2B) (*53*).

Histopathology was used to confirm the lack of Ω76 toxicity at maximum sublethal doses. Liver and kidney samples were extracted from Ω76- and colistin-treated mice from Fig. 2E (survivors and nonsurvivors) and compared to untreated controls (Fig. 2, G to L). Kidney histological samples for the control (Fig. 2G) and Ω76-treated (Fig. 2H)

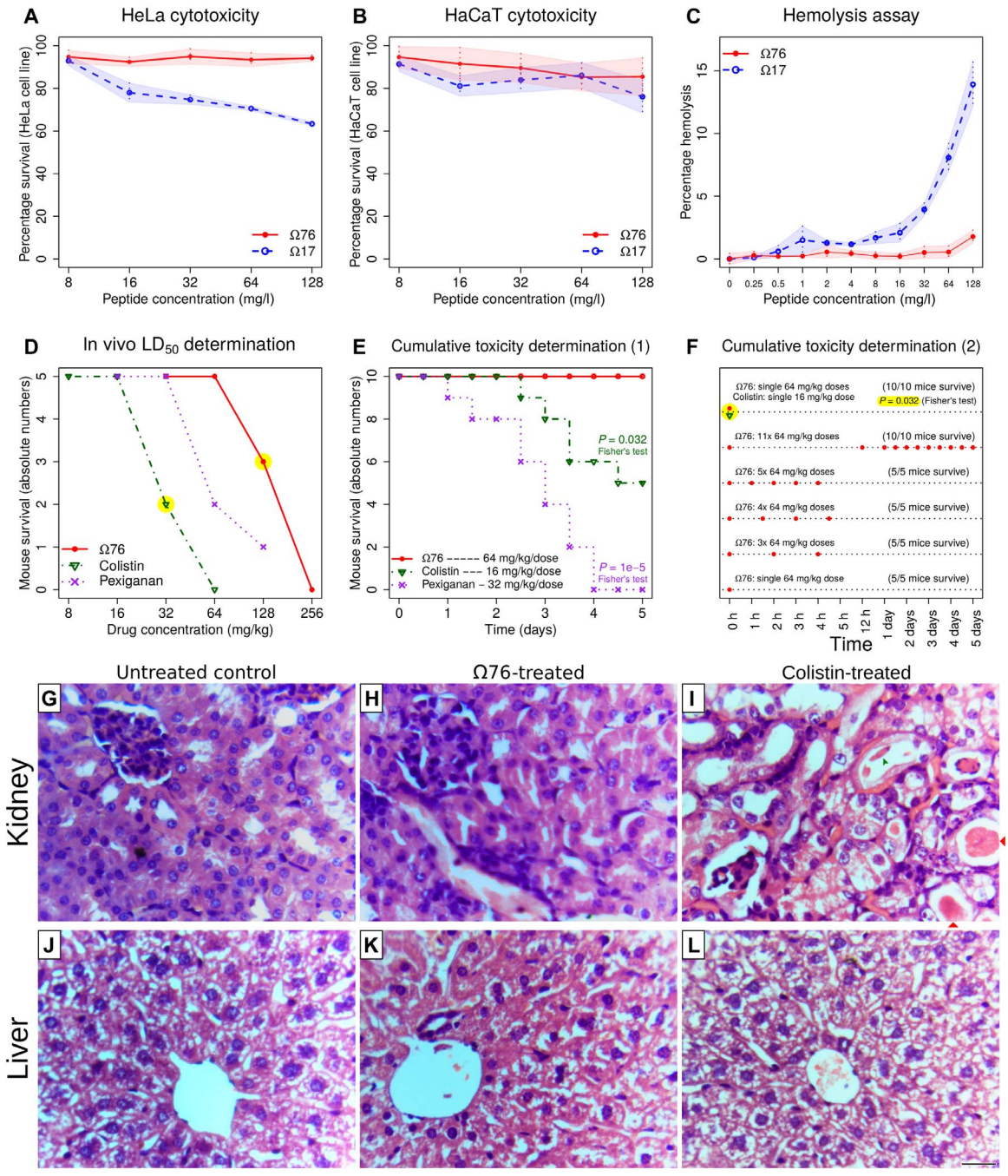

Fig. 2. In vitro and in vivo toxicity assessment of Ω76 and controls. (**A**) HeLa cell line toxicity for peptides Ω17 and Ω76. (**B**) HaCaT cell line toxicity for peptides Ω17 and Ω76. (**C**) Human blood hemolysis assay for peptides Ω17 and Ω76. (A to C) All experiments were performed in three to five replicates. Lines and shaded regions indicate means and SD, respectively. (**D**) In vivo LD_{50} (median lethal dose) determination for Ω76, pexiganan, and colistin using a BALB/c mouse model. (**E**) Multidose cumulative toxicity determination for Ω76, pexiganan, and colistin using a BALB/c mouse model. (**F**) Row 1: Ω76-colistin coadministration experiment. All data relevant to this experiment have been highlighted in yellow across all panels. Row 2: Ω76 multidose survival experiment [repeated from (E) for completeness]. Rows 3 to 5: Cumulative toxicity determination for Ω76 administered at different time intervals. Row 6: Ω76 single-dose survival experiment [repeated from (D) for completeness]. BALB/c mouse kidney and liver histological sections after treatment with Ω76 and controls. (**G**) Kidney from untreated mouse, displaying no damage. (**H**) Kidney from Ω76-treated mouse, displaying no damage. (**I**) Kidney from colistin-treated mouse. Cast formation (red arrowheads) and tubular necrosis (green arrowhead, dislodged cellular material) are both visible. (**J**) Liver from untreated mouse, displaying no damage. (**K**) Liver from Ω76-treated mouse, displaying no damage. (**L**) Liver from colistin-treated mouse, displaying no damage. Scale bar, 20 μm. All raw data for this figure are provided in dataset S1.

cohorts displayed no signs of injury, with renal tubules and glomeruli appearing intact. As expected, the colistin-treated cohort displayed extensive renal damage (Fig. 2I), with prominent tubular necrosis and cast formation clearly visible. Liver histological samples for all cohorts displayed no necrosis or lipid vacuolation typically associated with liver damage (Fig. 2, J to L). These results confirm that Ω76 has no nephrotoxic or hepatotoxic activity after multiple maximum sublethal doses.

Blood tests were used to further confirm the lack of Ω76 toxicity. The Ω76 cumulative toxicity experiment (Fig. 2E) was repeated with five mice, and blood was extracted at the end of 5 days. Serum creatinine, blood urea nitrogen, alanine aminotransferase, and alkaline phosphatase levels were assayed and compared to samples extracted from five untreated mice (fig. S3). In all cases, there was no significant difference between Ω76-treated and untreated cohorts. These results further confirm that multiple maximum sublethal doses of Ω76 produce no nephrotoxic or hepatotoxic effects.

Ω76 successfully treats infections of carbapenem- and tigecycline-resistant *A. baumannii* in a mouse peritoneal model of infection

We tested the in vivo efficacy of Ω76 using a BALB/c mouse peritoneal model of infection. Mice were infected with 3×10^7 colony-forming units (CFU) of a meropenem- and tigecycline-resistant *A. baumannii* (P1270) clinical isolate [species confirmed using 16*S* ribosomal RNA (rRNA) sequencing; table S6]. *A. baumannii* (P1270) was also deposited into the Microbial Type Culture Collection (MTCC culture number: 12889). Pilot experiments were performed to optimize Ω76 dosing (fig. S4).

Four cohorts consisting of eight infected mice each were used (Fig. 3A). The first cohort was left untreated. The second cohort was treated with three doses of Ω76: 32 mg/kg (13.77 μmol/kg), 16 mg/kg, and 16 mg/kg administered at 0.5, 2.5, and 4.5 hours, respectively, after infection. The third cohort was treated with a standard dose of 13.33 mg/kg (34.76 μmol/kg) meropenem administered at 0.5 hour after infection.

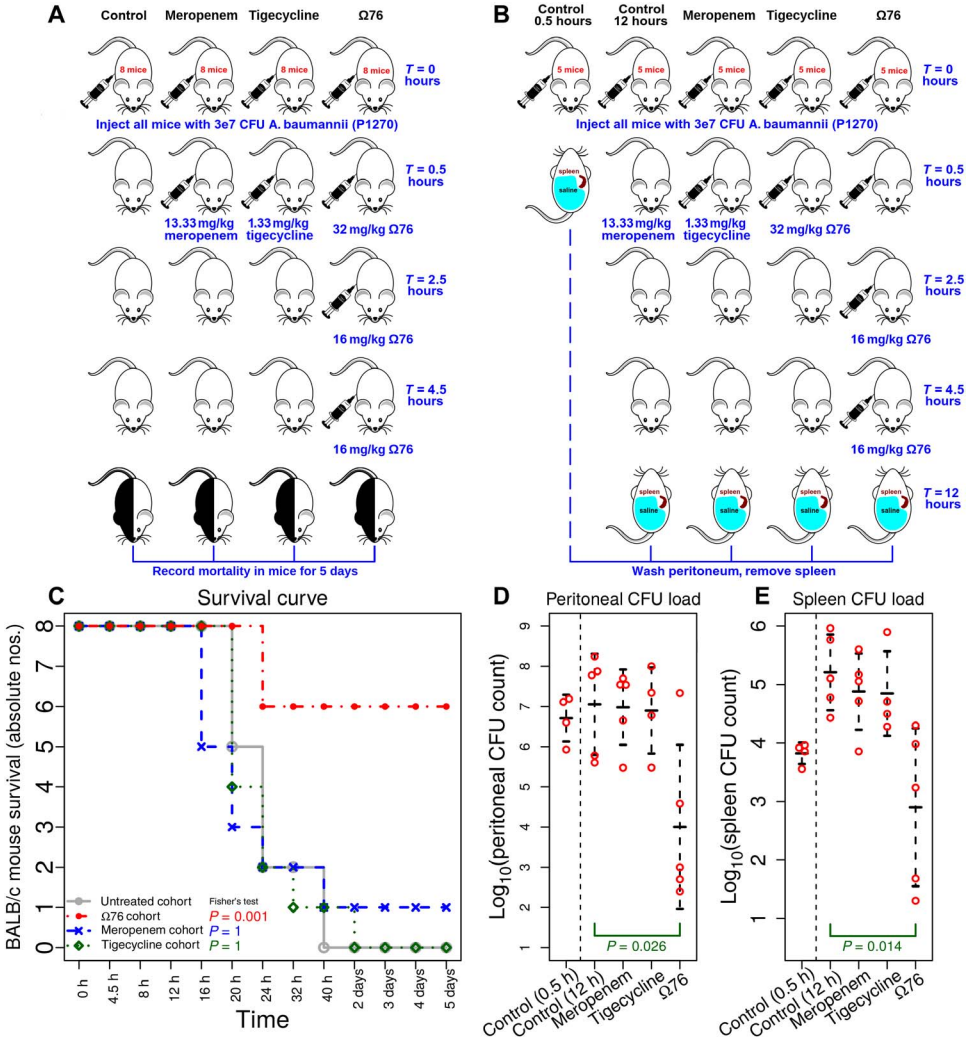

Fig. 3. In vivo efficacy of Ω76 using a BALB/c mouse peritoneal model of infection. (**A**) Protocol for the survival experiment to determine the efficacy of Ω76. (**B**) Protocol for peritoneal and spleen CFU estimation to determine the efficacy of Ω76. (**C**) Results of the survival experiment to determine the efficacy of Ω76, along with untreated, meropenem, and tigecycline controls (*P* values were calculated using Fisher's exact test). (**D**) Results of the peritoneal CFU estimation experiment to determine the efficacy of Ω76, along with untreated, meropenem, and tigecycline controls (*P* values were calculated using the Welch two-sample *t* test). (**E**) Results of the spleen CFU estimation experiment to determine the efficacy of Ω76, along with untreated, meropenem, and tigecycline controls (*P* values were calculated using the Welch two-sample *t* test). All raw data for this figure are provided in dataset S1.

The fourth cohort was treated with a standard dose of 1.33 mg/kg (2.27 μmol/kg) tigecycline administered at 0.5 hour after infection. Meropenem and tigecycline doses were based on U.S. Food and Drug Administration guidelines (*54*, *55*) for the treatment of an adult. All mice were monitored for 5 days after infection, and survival curves were plotted (Fig. 3C). Six of eight Ω76-treated mice survived for 5 days, significantly higher than the untreated survival rate of 0 of 8 ($P = 0.001$). In contrast, only one of eight meropenem-treated mice ($P = 1$) and zero of eight tigecycline-treated mice survived for 5 days. As *A. baumannii* (P1270) is meropenem- and tigecycline-resistant, poor performance of these drugs was expected. To confirm Ω76 efficacy, this experiment was independently replicated using uninfected and Ω76-treated cohorts using the same dosing regimen (eight mice each; fig. S5). Similar results were obtained, with six of eight of mice treated with Ω76 surviving in comparison to a one of eight survival rate of untreated mice ($P = 0.015$).

To further demonstrate the efficacy of Ω76 against *A. baumannii* (P1270), we performed peritoneal and spleen CFU counts using five cohorts of BALB/c mice (five mice per cohort) infected with 3×10^7 CFU of *A. baumannii* (P1270). The Ω76, meropenem, and tigecycline cohorts were treated with the same dosing regimen used for the previous survival experiment (Fig. 3B). For these cohorts, all mice were euthanized 12 hours after infection. Two control cohorts were used, where mice were euthanized at 0.5 and 12 hours after infection, respectively. In all cases, peritoneal washes and spleens were extracted immediately after euthanization.

Ω76 was found to significantly reduce *A. baumannii* (P1270) loads in both the peritoneum ($P = 0.026$, Fig. 3D) and spleen ($P = 0.015$, Fig. 3E). Ω76 reduced peritoneal loads >1000-fold, while spleen loads were reduced >100-fold. Meropenem and tigecycline did not significantly reduce *A. baumannii* (P1270) loads in the peritoneum (meropenem, $P = 0.920$; tigecycline, $P = 0.847$) or spleen (meropenem, $P = 0.448$; tigecycline, $P = 0.463$). Further, the mouse immune system was unable to reduce *A. baumannii* (P1270) loads. Peritoneal CFU counts remained constant at both 0.5 and 12 hours after infection. Spleen CFU counts increased >10-fold 12 hours after infection possibly due to our infection model, as *A. baumannii* (P1270) introduced peritoneally would require time to enter the bloodstream.

Ω76 localizes within and disrupts bacterial membranes, inducing small-molecule leakage, resulting in rapid bactericidal activity

Confocal microscopy experiments were performed to track Ω76 during its interaction with bacterial cells (Fig. 4). *E. coli* (K12 MG1655) and drug-resistant *A. baumannii* (P1270) were used for these experiments. Fluorescein isothiocyanate (FITC)–labeled Ω76, Nile red (a lipophilic cell membrane stain), and 4′,6-diamidino-2-phenylindole (DAPI) (a nucleic acid stain) were used to treat these isolates, and they were visualized immediately after staining. Ω76 was found to colocalize with Nile red for both *E. coli* (K12 MG1655) and *A. baumannii* (P1270), indicating immediate binding to the bacterial cell membrane.

Colocalization for both *E. coli* (K12 MG1655) and *A. baumannii* (P1270) was quantified using Pearson's correlation (Fig. 4, inset table). Stronger correlations indicated better colocalization. For both isolates, the strongest correlation was observed for Nile red/FITC-Ω76, confirming that the peptide selectively binds to bacterial cell membranes.

Time-kill kinetic experiments (Fig. 5A) were performed in ex vivo whole human blood for Ω76, colistin, and an untreated control. Concentrations corresponding to the clinical doses of Ω76 (32 mg/liter) and colistin (5 mg/liter) (*56*) were used. Ω76 rapidly reduced *A. baumannii*

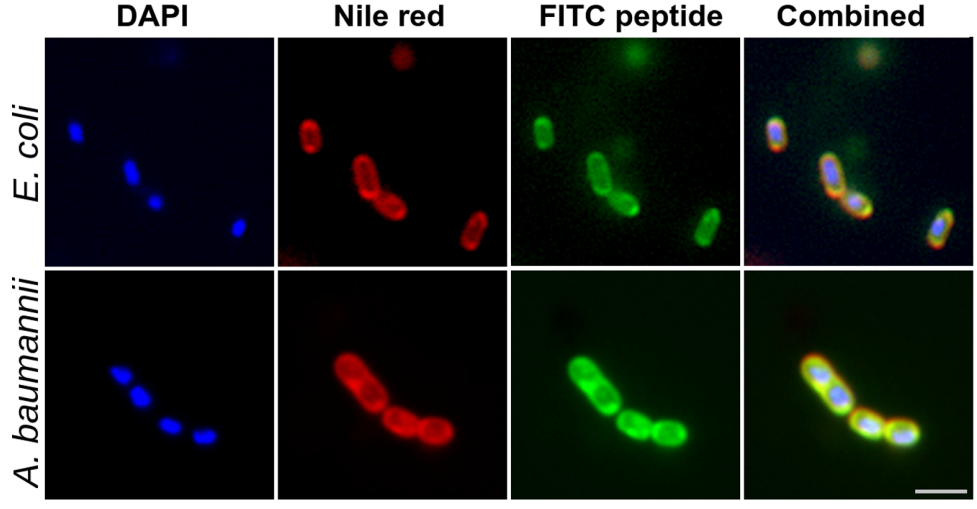

Culture	R/G	G/B	R/B			
E. coli	**0.46**	−0.20	−0.24	R	(RED channel)	Nile red stain
A. baumannii	**0.65**	−0.22	−0.06	G	(GREEN channel)	FITC-labeled peptide
				B	(BLUE channel)	DAPI stain

Fig. 4. Confocal microscopy experiments performed on *E. coli* (K12 MG1655) and *A. baumannii* (P1270). (**Top**) FITC-labeled Ω76-treated *E. coli*. Ω76 colocalized with Nile red, indicating a membrane-binding propensity. (**Bottom**) FITC-labeled Ω76-treated *A. baumannii* (P1270). Ω76 again colocalized with Nile red, indicating a membrane-binding propensity. (Table) Pearson's correlation coefficients given for all combinations of stains (DAPI/FITC peptide/Nile red). Better stain colocalization is denoted by higher correlation values. In both cases, the Nile red/FITC peptide pair was the most strongly correlated. Scale bar, 2 μm. Note that these images have been digitally magnified by 3× for clarity. All original images are provided in dataset S1.

(P1270) counts, causing a $\geq 10^5$-fold CFU reduction in 10 min and the complete elimination of all CFU in 60 min. Colistin treatment resulted in a more modest CFU reduction of 32-fold after 60 min. As expected, no CFU reductions were observed in the untreated control.

A radiolabeled phosphate release assay (Fig. 5B) was performed to help understand the cause of the rapid bactericidal activity of Ω76. Phosphate was used as a model small molecule to help trace the possible leakage of essential small molecules such as K^+/Na^+ ions, amino acids, and sugars during membrane disruption. Treatment with Ω76 caused rapid phosphate leakage. Thirty-three percent of intracellular phosphate was lost in 10 min, rising to a 57% loss in 60 min. Treatment with colistin causes slower phosphate leakage. Ten percent of intracellular phosphate is lost in 10 min, slowly rising to a 25% loss in 60 min. As expected, the untreated control lost the least amount of phosphate, losing only 10% after 60 min. Together, these three experiments indicate that Ω76 is rapidly incorporated into the bacterial cell membrane, creating membrane disruptions that permit the rapid leakage of cytoplasmic small molecules, resulting in immediate bacterial death.

We performed SEM experiments to determine the morphological changes induced by Ω76 on the bacterial cell membrane. Drug-resistant *A. baumannii* (P1270) displayed no morphological changes upon peptide treatment. We performed the same experiment for a sensitive strain of *A. baumannii* (B4505) and also observed no morphological changes (fig. S6). However, *A. baumannii* (B4505) protoplasts displayed some membrane irregularities at high magnifications (fig. S7). Clear membrane disruption was observed in *E. coli* (K12 MG1655), with prominent blebbing indicating the loss of structural cohesion of the cell membrane (fig. S8). Similar observations were recorded for *Shigella flexneri* (MTCC 1457), which showed membrane disruption followed by the loss of cytoplasmic contents (fig. S9). Note that large-scale membrane disruption was only observed after a 2-hour prolonged incubation period and with high concentrations of Ω76 (128 mg/liter). These results indicate that large-scale membrane damage is not a prerequisite for bacterial death, which occurs on much shorter time scales. However, these observations still confirm the direct interaction of Ω76 with bacterial membranes.

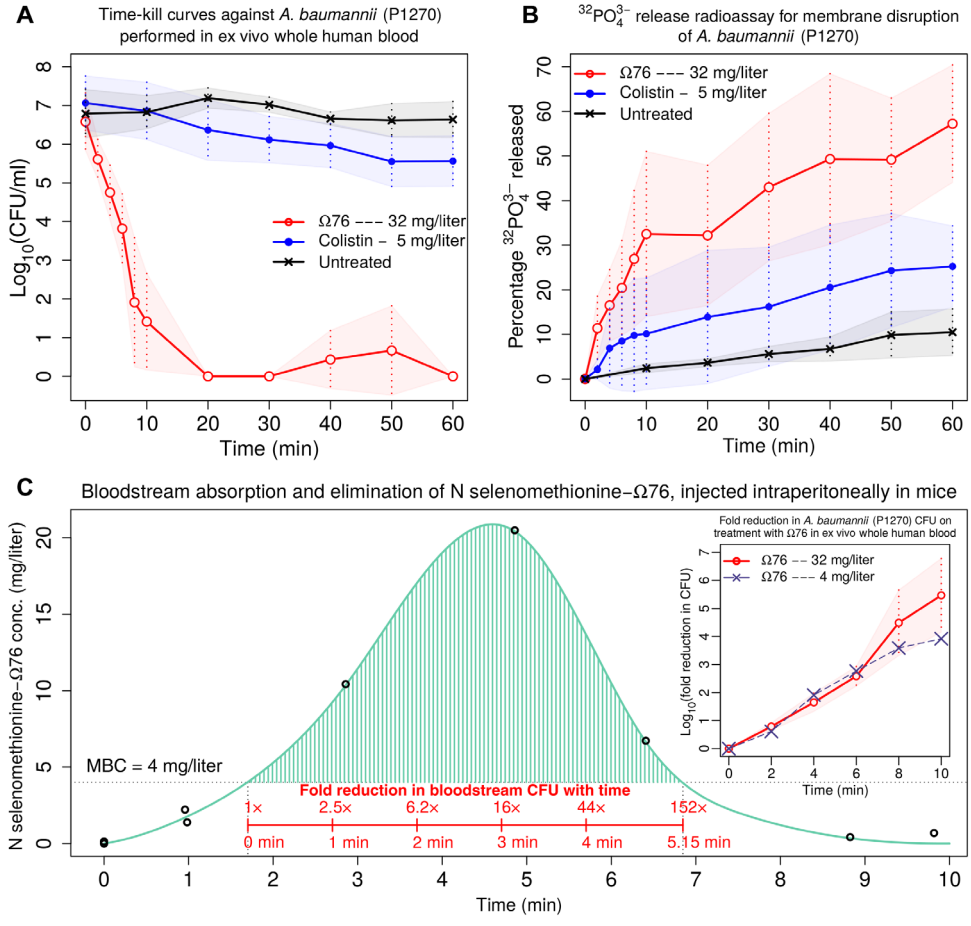

Fig. 5. The time-kill kinetics and elimination kinetics of Ω76. (**A** and **B**) Kinetic experiments showing the rapid action of Ω76 on *A. baumannii* (P1270). All experiments in these panels were performed in triplicate. (A) Time-kill curves performed on *A. baumannii* (P1270) treated with clinically relevant doses of Ω76, colistin, and an untreated control. These experiments were performed in ex vivo whole human blood. (B) $^{32}PO_4^{3-}$ release radioassay to detect the leakage of small molecules upon incubation of *A. baumannii* (P1270) with Ω76, colistin, and an untreated control. (**C**) Pharmacokinetic experiments performed on mice to determine the bloodstream absorption and elimination kinetics of peritoneally injected Nselmet-Ω76. Curve fitting was performed using spline interpolation. The shaded area corresponds to Nselmet-Ω76 serum concentrations above the MBC. Inset: Fold reduction curves for Ω76, performed on *A. baumannii* (P1270) in ex vivo whole human blood. The fold reduction curve for Ω76 at 32 mg/liter is derived from the same data displayed in (A). The fold reduction curve for Ω76 at MBC (4 mg/liter) closely follows the trend at 32 mg/liter up to 6 min. However, Ω76 at MBC is unable to continue reducing *A. baumannii* (P1270) CFU counts, diverging from the 32 mg/liter trend at 8 min. For all experiments, lines and shaded regions indicate means and SD, respectively. All raw data for this figure are provided in dataset S1.

Of particular interest are the in vivo killing kinetics of Ω76, especially within the bloodstream. Previously described experiments have already established the ability of Ω76 to markedly reduce *A. baumannii* (P1270) peritoneal and spleen CFU loads in mice (Fig. 3, D and E), indicating similar in vivo and ex vivo killing kinetics. In addition, pharmacokinetic experiments were performed (Fig. 5C) to understand the absorption and elimination kinetics of Ω76 within the mouse bloodstream. For these experiments, Ω76 was labeled with an N-terminal selenomethionine probe, which did not affect the peptide's MBC against *A. baumannii* (table S5). BALB/c mice were intraperitoneally injected with Nselmet-Ω76 (70 mg/kg). At different time points, blood from individual mice was extracted via terminal cardiac puncture. The serum selenium content was then quantified via inductively coupled plasma mass spectrometry (ICP-MS), which was a direct measure of Nselmet-Ω76 concentration. We observed that Nselmet-Ω76 reached a peak serum concentration of 20 mg/liter at 4.5 min after injection and was completely eliminated 10 min after injection. The concentration of Nselmet-Ω76 in the bloodstream remained greater than the MBC (4 mg/liter) of *A. baumannii* (P1270) for 5.15 min. From previous time-kill experiments performed in ex vivo whole human blood (Fig. 5A; also represented in Fig. 5C, inset, in fold reduction terms), we observed that 5.15 min was sufficient for a 152-fold CFU reduction, sufficient to significantly improve survival outcomes. Of course, because of the noncumulative toxicity of Ω76 (Fig. 2, E and F), multiple doses can be administered to achieve any target CFU reduction.

The molecular response of *A. baumannii* to Ω76 challenge

Drug-resistant *A. baumannii* (P1270) was challenged with Ω76 at concentrations of 0.1×, 0.25×, and 0.5× MBC [Gene Expression Omnibus (GEO) accession number: GSE116245]. Differentially expressed genes (DEGs) displaying a 1.5-fold change (up- or down-regulation) for all MBC concentrations and belonging to significantly overrepresented Gene Ontology (GO) terms were identified, as described in Methods. Using these measures, 134 genes (GO-up) were up-regulated and 62 genes (GO-down) were down-regulated upon Ω76 treatment over an MBC concentration range of 0.1 to 0.5×. Up-regulated genes (GO-up; table S7) were classified under 16 GO terms, while down-regulated genes (GO-down) were classified under 4 GO terms (GO-down; table S8). A graphical representation of the features and relationships between GO terms is provided in fig. S10.

The molecular response is depicted in Fig. 6. Genes associated with 67 inner membrane proteins (and 4 outer membrane proteins) were found to be significantly up-regulated, and only 4 membrane-associated genes were down-regulated. The significant up-regulation of diverse membrane proteins may be required to compensate for Ω76-induced membrane damage.

Twenty-two membrane-associated genes belonging to membrane transport proteins were up-regulated. Transporters for H_2O, H^+, K^+, Na^+, NH^{4+}, Fe, and Zn ions were up-regulated, which is a response expected to compensate for Ω76-induced rapid small-molecule leakage (Fig. 5B). Transporters for organic small molecules such as α-ketoglutarate,

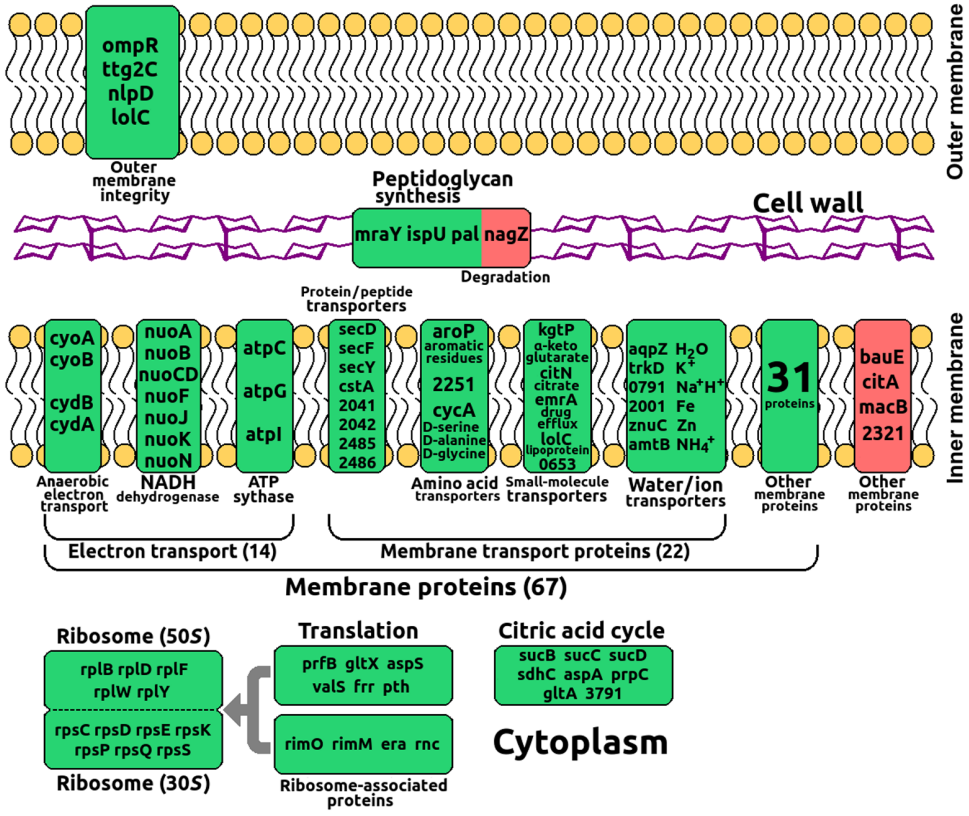

Fig. 6. The molecular response of *A. baumannii* (P1270) to Ω76 challenge. Up- and down-regulated (GO-up and Go-down) genes are colored green and red, respectively. For clarity, only DEGs belonging to GO terms with biological functions relevant to this study are shown. A full list of DEGs can be found in tables S4 and S5. Note that some genes can have multiple functions and belong to multiple GO terms. Note that some genes do not have corresponding gene names assigned. In these cases, the truncated Agilent ID has been used. For example, "2251" mentioned in the above figure corresponds to Agilent ID ABAYE2251.

citrate, serine, alanine, glycine, and aromatic residues were also up-regulated, indicating possible leakage of these compounds as well.

Fourteen membrane-associated genes belonging to electron transport chain components—NADH (reduced form of nicotinamide adenine dinucleotide) dehydrogenase (seven genes), adenosine triphosphate (ATP) synthase (three genes), and anaerobic electron transport components (four genes)—were up-regulated. It is possible that these genes are up-regulated in response to Ω76-induced displacement of periplasmic H^+ ions, which are required for ATP synthesis.

Other genes belonging to diverse metabolic pathways were also found to be up-regulated, hinting at metabolic inhibitory processes. It should be noted that Ω76-induced metabolic inhibition would occur on longer time scales than simple membrane disruption and would only be relevant under circumstances where sub-MBC concentrations of Ω76 are used.

Four genes (*ompR*, *ttg2C*, *nlpD*, and *lolC*) responsible for maintaining outer membrane integrity and three genes (*mraY*, *ispU*, and *pal*) responsible for cell wall synthesis were also up-regulated. *nagZ*, responsible for peptidoglycan degradation, was down-regulated.

Twelve genes belonging to ribosomal proteins (5 genes for 50*S* subunit and 7 genes for 30*S* subunit) were up-regulated. Six genes involved with translation, and four genes associated with other ribosome-associated processes, were also up-regulated. Further, eight genes associated with the citric acid cycle were also up-regulated. The up-regulation of ribosomal proteins and components of the citric acid cycle may be a product of increased metabolic demands in response to Ω76 treatment. Alternatively, AMPs are known to trap ribosomal release factors (*29*), inhibit ribosomal protein synthesis (*27*, *28*), and cause ribosomal aggregation (*32*). It is therefore conceivable that the up-regulation of ribosomal proteins is a response to ribosomal inhibition caused by Ω76.

Some GO terms included poorly characterized genes (such as transcriptional regulators with no known targets for GO:0003677 and GO:0006355) or contained diverse genes with little commonality (such as enzymes with unknown reactants/products for GO:0008152, GO:0016740, GO:0005524, and GO:0005737). In these cases, the contributions of these genes to the molecular response of *A. baumannii* remain unclear.

Ω76 adopts an α-helical structure in apolar solvents

Ω76 in 100% CD_3OH was observed to have some helical content, as evidenced by several H^N-H^N nuclear Overhauser effects (NOEs), characteristic of α helices, which were observed in the spectrum. Eight H^N_i-H^N_{i+1}, three H^N_i-H^N_{i+2}, and one H^N_i-H^N_{i+4} correlations were observed (Fig. 7C). Additional correlations may have been obscured because of spectral artifacts close to the diagonal. The upfield shift of Hα resonances, so that they appear between 3.5 and 4.5 ppm, also points to α-helical content. However, the lack of adequate nonsequential NOEs and poor chemical shift dispersion prevented the calculation of the solution structure in this condition.

Ω76 was then prepared in membrane-mimetic deuterated dodecylphosphocholine (DPC; D38) micelles. The spectral characteristics in the presence of DPC showed a marked improvement over the sample in methanol, with improved chemical shift dispersion, as well as improved transfer of the NOE. Eighteen H^N_i-H^N_{i+1} correlations and 16 weaker H^N_i-H^N_{i+2} correlations were observed (Fig. 7D), strong evidence that the entire length of the peptide adopts an α-helical conformation. Raw NOESY (nuclear Overhauser effect spectroscopy)/TOCSY (total correlation spectroscopy) spectral data in all solvents are provided in dataset S3.

The sequential and medium-range NOEs as well as secondary chemical shifts and the chemical shift index (CSI) are summarized in Fig. 7E. The first three rows depict sequential NOE connectivities, where the thickness of the bar indicates a weak, medium, or strong NOE. The next five rows depict medium-range NOEs characteristic of α-helical structures, where a connecting line indicates that the two residues are connected by an NOE. The next row depicts secondary chemical shifts for H^α. Here, a negative value denotes an upfield shift with respect to random coil values and is indicative of an α-helical structure. The next row depicts the CSI. The CSI is calculated by applying a residue-specific digital filter to the secondary chemical shift, where −1 indicates an α helix, 0 indicates a random coil, and +1 indicates a β strand. Last, the secondary structure assigned on the basis of NOEs and CSI is provided in the last row.

An ensemble of 30 structures was calculated using this NOE and chemical shift data [Fig. 7F,left; PDB (Protein Data Bank) coordinates in text S1]. All backbone dihedral angles fell within the favorable region of the Ramachandran plot (fig. S11). Figure 7F also depicts a view down the helix axis, with hydrophobic residues colored white (Ala, Gly, Ile, Leu, and Phe), negatively charged residues colored red (Glu), and positively charged residues colored blue (Lys). It is evident that the residues are not evenly distributed but are clustered on the basis of their hydrophobicity. Restraints used for structure calculation and structure statistics are summarized in table S9. The electrostatic surface potential and 3D hydrophobic moment (3D-HM) vector calculated for the first model of the ensemble are shown in fig. S12. The angle between the helix axis and the hydrophobic moment vector is 33.3°, and the absolute value of the vector is 47.816 kTÅ/e.

DISCUSSION

The proliferation of drug-resistant pathogens over the past few decades has created an urgent need for new antibiotics. The ESKAPE pathogen family is particularly concerning, as its members are increasingly displaying resistance to carbapenem class antibiotics. Treatment options for carbapenem-resistant infections are limited to drugs of last resort such as tigecycline and colistin. Unfortunately, both drugs have significant drawbacks: The prevalence of tigecycline resistance continues to increase (*14*), while colistin displays nephrotoxic effects after prolonged treatment (*16*–*18*).

In this study, we used a maximum common subgraph computational approach to design AMPs (Fig. 1). α-Helical AMP structures extracted from the APD (*49*) were reduced to graphical representations. Residues were reduced to nodes, while intra-residue covalent and backbone hydrogen bonds were reduced to connecting edges. We then attempted to design new AMPs by maximizing the number of subgraphs shared between a given design and existing AMPs. Our method was based on the hypothesis that commonly occurring structural subgraphs would be evolutionarily conserved only if they bestowed their parent peptides with greater antimicrobial activity. We tested this hypothesis by generating shuffled variants of Ω76 (Ω76-shuf1→4; Table 1) using an inverted Heligrapher energy function that removed all subgraphical motifs shared with known AMPs. These peptides displayed significantly lower activity in comparison to Ω76 (table S5), thereby validating our hypothesis.

Ω76 has a remarkable safety profile. Multiple Ω76 doses can be administered intraperitoneally to mice over a clinically relevant time scale of 5 days without any noticeable adverse effects (Fig. 2, E and F). In contrast, repeated maximum sublethal doses of pexiganan caused

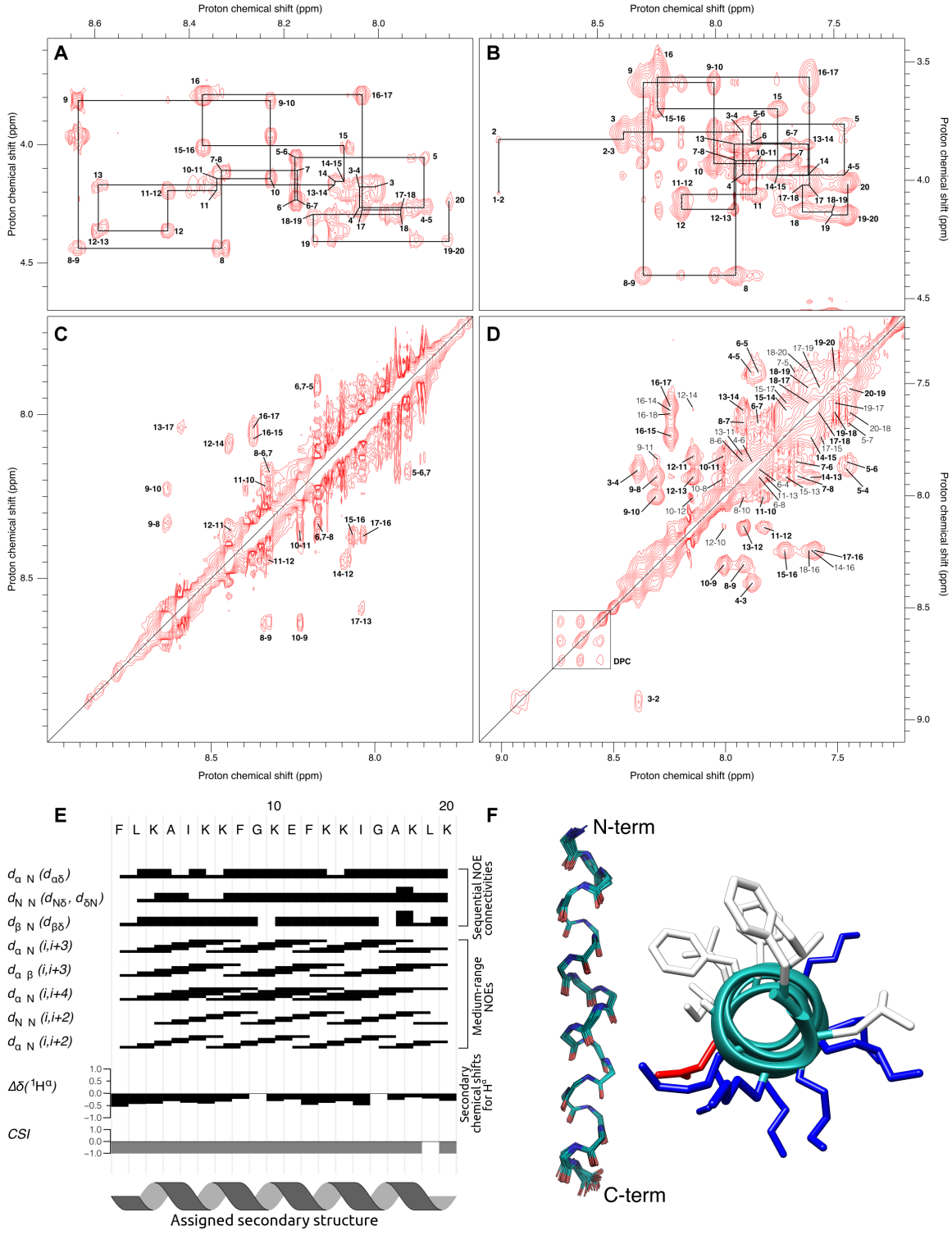

Fig. 7. Calculation of the solution structure of Ω76 in the presence of DPC micelles. Sequential assignments were carried out using the H^N- H^α region of the $^1H,^1H$-NOESY spectra of Ω76 (**A**) in 100% CD_3OH and (**B**) in 25 mM DPC (D38) in 90%/10% H_2O/D_2O. The labels are of the form *x*-*y* or *z*, where *x* is the residue number of the H^α resonance, *y* is the residue number of the H^N resonance, and *z* is an intra-residue correlation (*x* = *y*). (**C**) H^N-H^N region of the $^1H,^1H$-NOESY spectra of Ω76 in 100% CD_3OH and (**D**) in 25 mM DPC (D38) in 90%/10% H_2O/D_2O. The labels indicate the residue numbers of the H^N resonances involved in the correlation. Eighteen H^N_i-H^N_{i+1} correlations are observed and labeled in bold, while 14 of 16 weaker H^N_i-H^N_{i+2} correlations are also shown. The remaining two H^N_i-H^N_{i+2} correlations are seen at lower contour levels and are therefore not labeled. (**E**) Summary of the NOE and chemical shift data used for assigning the secondary structure as a function of residue number. (**F**) Ensemble of 30 calculated structures (left) and view down the helix axis (right). The side-chain colors indicate hydrophobic (white), acidic (red), and basic (blue) residues.

100% mortality in mice (Fig. 2E), indicating that it is unfit for internal use (it should be noted that the toxicological experiments described in this work cannot be used to assess the suitability of pexiganan as a topical agent, an application where internal toxicity is unimportant). These results are interesting as the amino acid compositions of Ω76 and pexiganan share some similarities (Table 1). Both are short lysine-rich peptides with a similar charge and hydrophobicity profile. The extreme differences in their cumulative toxicities must therefore arise from subgraphical or structural differences. Other AMPs also have toxicological characteristics that render them unsuitable for internal administration. For example, gramicidin S (*46*), melittin (*47*), and lactoferrampin (*48*) display hemolytic properties. Therefore, the toxicological properties of Ω76 are unique even among AMPs.

Furthermore, repeated maximum sublethal doses of colistin, a widely used antibiotic, caused 50% mortality in mice (Fig. 2E) and observable renal damage (Fig. 2I). These results are interesting as colistin is known to be nephrotoxic across diverse patient cohorts. Recent studies have shown that colistin usage caused acute kidney injury in 46.1% of a Turkish elderly patient cohort (*16*) and 54.6% of a Korean elderly patient cohort (treated for ≥72 hours) (*17*). Another study at the Walter Reed Army Medical Center (*18*) using a young patient cohort reported acute kidney injury in 45% of patients and the cessation of colistin treatment in 21% of patients due to nephrotoxicity. As Ω76 has no nephrotoxic properties, it has the potential to supplement or replace colistin in clinical settings. Simultaneous maximum sublethal doses of Ω76 and colistin could be coadministered intraperitoneally to mice without any observed mortality, indicating that their toxic effects are noncumulative.

Besides toxicity, rapid elimination kinetics also limit the clinical use of AMPs. This is especially true if significant time-kill CFU reductions take longer than an AMP in vivo availability. Fortunately, although the serum concentration of Ω76 remains above the MBC of *A. baumannii* (P1270) for 5.15 min, its rapid bactericidal activity allows a 152-fold CFU reduction (Fig. 5C) within that same time. This gives Ω76 an advantage over slower-acting conventional antibiotics such as colistin and meropenem, as it produces similar CFU reductions in much shorter time periods. A clinical dose of colistin remains above MIC concentrations in mouse serum for 100 min (*57*) but only produces a 32-fold reduction in CFU over 60 min (Fig. 5A). Similarly, a clinical dose of meropenem remains above MIC concentrations in the serum of human volunteers for 5 hours (*58*) but only displays a 100-fold CFU reduction in 4 hours (*59*).

The efficacy of Ω76 was tested using a mouse peritoneal model of infection against meropenem- and tigecycline-resistant *A. baumannii* (P1270). Untreated, Ω76-treated, meropenem-treated, and tigecycline-treated cohorts of mice were used. Only the Ω76-treated cohort displayed a significant improvement in survival outcomes (Fig. 3C) and a significant decrease in peritoneal and spleen bacterial loads (Fig. 3, D and E). To the best of our knowledge, Ω76 represents the only post-colistin compound reported to display in vivo efficacy against tigecycline-resistant pathogens. To ensure the reproducibility of our results, A.D. independently replicated our findings in a different laboratory, and without supervision by any other authors of this study (fig. S5). We have also deposited *A. baumannii* (P1270) into the Microbial Type Culture Collection (MTCC culture number: 12889) for easy access to the community.

We performed a variety of experiments to understand the mechanism of action of Ω76. Ω76 was found to localize within bacterial cell membranes (Fig. 4), causing disruptions that induced rapid small-molecule leakage (Fig. 5B), which resulted in rapid bactericidal activity (Fig. 5A). Genes for small-molecule transporters were also found to be significantly up-regulated upon treating *A. baumannii* (P1270) with Ω76 (Fig. 6).

NMR experiments indicate that Ω76 adopts an α-helical conformation upon interacting with DPC micelles and, by extension, the lipid membrane. Membrane-interacting peptides have previously been shown to be amphipathic in nature (*60*), having one hydrophobic and one hydrophilic surface. The electrostatic surface potential calculated for the Ω76 model shows the amphipathic nature of the peptide in its folded state, with one positively charged and one hydrophobic face (fig. S12A). The 3D-HM vector indicates the most likely membrane-interacting surface of the peptide (fig. S12B). Although the 3D-HM vector cannot be used to predict the orientation of the peptide in the membrane, anecdotal evidence (*61*) suggests that Ω76 may interact with the membrane in such a way that the vector becomes parallel to the membrane normal. Assuming a horizontally oriented planar membrane, the orientation shown in fig. S12B therefore represents the likely orientation of the peptide with respect to the membrane as predicted by the 3D-HM vector. Because the angle between the calculated vector and the helix axis is only 33.3°, it is possible that the peptide not only interacts with the membrane surface but also may become embedded in the membrane to some extent. Small-molecule leakage and the 3D-HM vector suggest that Ω76 may act through the formation of pores.

The simultaneous efficacy and low toxicity of Ω76 are unique properties that, to the best of our knowledge, have not been reported for any compound (experimental or commercial) displaying efficacy against carbapenem- and tigecycline-resistant organisms. Ω76 therefore appears to be a promising drug candidate, and future work will involve its development into a clinical therapeutic.

METHODS

Peptide synthesis

All peptides synthesized for this study were purchased from GenScript Inc. Initially for in vitro characterization, 20 mg of the five Ω-family peptides was purchased as part of a crude peptide library from GenScript Inc. Later, Ω17 (100 mg, >95% purity), Ω76 (1 g, >95% purity), and pexiganan (100 mg, >95% purity) were purchased separately for in vitro and in vivo experiments. FITC-labeled Ω17 (>95% purity) and FITC-labeled Ω76 (>95% purity) were purchased separately for confocal microscopy experiments.

Antimicrobial susceptibility assays

MICs were determined by the microwell dilution method, as described by Wiegand *et al.* (*62*) (Protocol E: Broth microdilution for AMPs that do not require the presence of acetic acid/bovine serum albumin). This method assays growth using optical density measurements (λ = 625 nm). This method was used to determine the efficacy of our peptides against a panel of 30 type cultures (table S2).

Most of our clinical isolates displayed mucoid or plaque morphologies, and growth could not be assayed using optical density readings. Instead, a modified protocol using resazurin was used to determine the efficacy of our peptides against 64 clinical isolates (Table 2). Resazurin, a weakly fluorescent dye, is reduced to fluorescent resorufin in direct proportion to microbial aerobic respiration. Microbial cultures were incubated at 37°C for 12 hours in 96-well polypropylene plates. Thirty microliters of a 0.02% (w/v) aqueous resazurin solution was then pipetted into each well. Further, incubation at 37°C was performed for

12 hours. Growth estimation was then performed on the basis of fluorescence ($\lambda_{excitation}$, 530 nm; $\lambda_{emission}$, 590 nm). Because aerobic respiration also occurs in bacteriostatic cultures, the lack of aerobic respiration indicates bactericidal activity. Therefore, the resazurin assay measures the MBC.

Hemolysis assay

Experiments were performed to determine whether the designed peptides had hemolytic activity. RBCs from human blood were extracted (removing white blood cells and platelets), suspended in nutrient medium at a concentration of 10^6 RBC/μl, and stored at 4°C. Peptides were tested for hemolysis at a concentration range of 0.25 to 128 mg/liter, using a 10-fold RBC dilution (10^5 RBC/μl), in a solution made up to 100 μl using phosphate-buffered saline (PBS). A positive (lysis) control consisting of RBCs lysed using distilled water (DW) and a negative control consisting of RBCs incubated in PBS were also prepared. These peptide-RBC solutions and controls (12 tubes total) were incubated at 37°C for 1 hour, followed by centrifugation at 3000 rpm for 5 min. The supernatant (80 μl) was pipetted and introduced into a polystyrene 96-well plate containing 80 μl of DW (160 μl total). Using colorimetry, the absorbance difference Δabs of all wells was calculated as follows

$$\Delta\text{abs} = \text{absorbance}\ (570\text{nm}) - \text{absorbance}\ (620\text{nm})$$

Absorbance at 570 nm is hemoglobin specific. Subtracted absorbance at 620 nm is nonspecific. The Δabs values of all wells were compared to a standard curve to determine percentage hemolysis. The steps for this hemolysis assay are depicted in fig. S13. For any given AMP, the entire protocol described in this section was repeated in triplicate to determine hemolytic activity.

Cell culture and cytotoxicity assay

HaCaT and HeLa human cell lines were grown in Dulbecco's modified Eagle's medium supplemented with 10% fetal bovine serum, streptomycin, gentamycin, and penicillin. Cells were incubated in this medium in cell culture flasks at 37°C in 5% CO_2 until 80 to 90% confluence was reached. These cells were later extracted using papain and used for cytotoxicity assays.

We used the 3-(4,5-dimethylthiazol-2-yl)-2,5-diphenyltetrazolium bromide (MTT) assay for the evaluation of the cytotoxic effects of Ω-family peptides. Polystyrene 96-well plates were seeded with 1×10^4 cells per well in 200-μl medium. Incubation was performed at 37°C for 12 hours in 5% CO_2, after which cells were exposed to peptides at twofold concentration increments. MTT at a final concentration of 500 mg/liter was added to each well and incubated for 4 hours. The supernatant was aspirated, 150 μl of dimethyl sulfoxide was added, and the cells were incubated for 10 min. Absorbance measurements at 570 nm were performed using the Multi-Mode Microplate Reader (BioTek, Vermont, USA). Results in the form of percentage growth were reported. Here, percentage growth is defined as the growth of cells exposed to peptide relative to unexposed control cells, cultured under identical conditions. Three to five replicates for all peptide concentrations were performed. Mean percentage growth and SD values were calculated for these replicates.

Checkerboard assay

We evaluated whether Ω76 and colistin have any synergistic, additive, or antagonistic effects on *A. baumannii* (P1270) using the checkerboard assay. This was performed by calculating the fractional inhibitory concentration (ΣFIC; Eq. 2) for a given combination of antibiotics.

$$\begin{aligned} \sum\text{FIC} &= \text{FIC}_{\text{colistin}} + \text{FIC}_{\Omega 76} \\ \text{FIC}_{\text{colistin}} &= \frac{\min(\text{MBC}_{\text{colistin}}\ \text{value oncheckerboard})}{\text{MBC}_{\text{colistin}}} \\ \text{FIC}_{\Omega 76} &= \frac{\min(\text{MBC}_{\Omega 76}\ \text{value oncheckerboard})}{\text{MBC}_{\Omega 76}} \end{aligned} \quad (2)$$

Here, $\sum\text{FIC} \leq 0.5$ indicates synergy, $0.5 < \sum \text{FIC} \leq 4$ indicates an additive effect, and $\sum\text{FIC} > 4$ indicates antagonism (*53*).

A checkerboard assay was performed on a 96-well polypropylene plate. Each well contained 200 μl of Mueller-Hinton medium, differing concentrations of antibacterial agents, and an inoculum of 5×10^4 CFU per well of *A. baumannii* (P1270), as depicted in fig. S2A. The 96-well checkerboard assay was incubated at 37°C for 12 hours. Thirty microliters of a 0.02% (w/v) aqueous resazurin solution was then pipetted into each well. Further incubation was performed at 37°C for 12 hours. Growth was estimated on the basis of fluorescence measurements (excitation, 530 nm; emission, 590 nm). The ∑FIC value for the chosen antibiotic combination was then estimated on the basis of bacterial growth.

In vivo toxicity experiments

In vivo toxicity experiments were performed for Ω76 along with untreated, colistin (colistin sulfate salt; Sigma C4461-100MG, lot no. SLBT0851), and pexiganan (custom synthesis; GenScript) controls, using the BALB/c mouse model. Two types of experiments helped assess peptide in vivo toxicity: (i) mouse survival experiments upon single-dose AMP treatment and (ii) mouse survival experiments upon multidose AMP treatment.

For single-dose AMP treatment, 6- to 8-week-old BALB/c mice weighing 20 g were intraperitoneally injected with Ω76, colistin, and pexiganan suspended in saline at concentrations ranging from 8 to 256 mg/liter. Four concentrations were tested for each compound, and five mice were used for each concentration (60 mice total). Mice were housed at the Central Animal Facility (CAF; IISc) and provided with pellet feed and water ad libitum. All mice were monitored for 5 days after injection, and any deaths occurring during this time period were noted. All mice were euthanized after this time period by ketamine overdose. LD_{50} estimation was performed using linear interpolation.

For another experiment, simultaneous sublethal doses of Ω76 (64 mg/kg) and colistin (16 mg/kg) were intraperitoneally injected into 10 mice to determine whether their toxic effects are additive. All mice were monitored for 5 days after injection, and any deaths occurring during this time period were noted. All mice were euthanized after this time period by ketamine overdose.

For multidose drug treatment, 30 BALB/c mice (10 per cohort) were intraperitoneally injected with a sublethal drug concentration (64 mg/kg for Ω76, 32 mg/kg for pexiganan, and 16 mg/kg for colistin) suspended in saline, every 12 hours for 5 days. Eleven doses were injected in total, and all mortality was recorded. Mice were euthanized immediately after the last dose to capture acute toxic effects. Liver and kidney samples were extracted from all mice, including those that failed to survive the entire drug treatment regimen. Additional multidose treatment experiments were performed by injecting Ω76 (64 mg/kg) at differing reduced time intervals to determine the safe dosing interval.

The multidose drug treatment experiment was repeated for Ω76. For five mice, the peptide (64 mg/kg) was injected intraperitoneally every 12 hours for 5 days. At the end of this period, mice were euthanized

using a terminal ketamine overdose, and blood samples were extracted via cardiac puncture. Blood samples of these five mice were tested for serum creatinine, blood urea nitrogen, alanine aminotransferase, and alkaline phosphatase levels and compared to blood extracted from five untreated mice.

Mouse peritoneal model of infection

For testing the efficacy of Ω76 and other control antibiotics, an *A. baumannii* (P1270) dose of 10^7 CFU from a 24-hour old culture was used (based on survival titration data; fig. S14). The CFU doses were quantified using turbidometry and retrospectively confirmed using colony plating. This infectious dose was administered at 0 hours. Mice were divided into untreated, Ω76-treated, meropenem-treated, and tigecycline-treated cohorts. Meropenem (batch no. FUD16008, Emcure Pharmaceuticals Ltd.) and tigecycline (batch no. 6BS16045, Gufic Biosciences Ltd.) were used to confirm *A. baumannii* drug resistance in vivo. At 0.5, 2, and 4 hours after infection, different agents were administered. Conventional antibiotics were only administered once at 0.5 hour after infection [meropenem (13.33 mg/kg) and tigecycline (1.33 mg/kg)]. Ω76 was administered at all three time points, with dosing regimens ranging from 16 to 32 mg/kg peptide injected intraperitoneally. In all cases, antibacterial agents were suspended in 200 μl of saline. All mice were observed for 5 to 7 days, and deaths were noted. All mice were euthanized by CO_2 overdose after this time interval. Upon plotting survival curves, *P* values to determine the efficacy of a given antimicrobial agent were calculated using Fisher's exact test.

A similar experiment was performed to estimate peritoneal and spleen CFU loads in untreated and antibiotic-treated mice. However, for this experiment, mice were euthanized 12 hours after infection via CO_2 overdose. Peritoneal washes were collected by injecting 5 ml of chilled saline into the peritoneum, followed by gentle massaging and aspiration. Similarly, spleens were extracted and washed in excess saline before homogenization. For both sample types, serial dilutions in saline and plating in Mueller Hinton agar containing meropenem (8 mg/liter) were immediately performed.

For all experiments, mice were housed at the CAF (IISc) and provided with pellet feed and water ad libitum. All animal experiments described in this work were approved by the Institutional Animal Ethics Committee, IISc (Project No. CAF/Ethics/550/2017).

Time-kill curves

Time-kill curves were performed for Ω76 (4 and 32 mg/liter), colistin (5 mg/liter), and an untreated control, against *A. baumannii* (P1270), in whole human blood.

An *A. baumannii* (P1270) culture was prepared in 10 ml of Mueller Hinton medium supplemented with meropenem (8 mg/liter) grown at 37°C/24 hours at 180 rpm. Whole human blood was freshly collected from D.N. via venipuncture in EDTA Vacutainer tubes (purple top). Approximately 10^7 CFU from this culture (33 μl), corresponding to the in vivo infective dose, was added to human blood such that the total volume was 1 ml (tube A). Separate experiments were performed to estimate CFU reductions at short time points (0, 2, 4, 6, 8, and 10 min) and long time points (0, 10, 20, 30, 40, 50, and 60 min). In all cases, Ω76 [32 mg/liter: 1.6 μl from a stock (20 mg/ml) in DW; 4 mg/liter: 2 μl from a stock (2 mg/ml) in DW] or colistin [0.5 μl from a stock (10 mg/ml) in DW] was only introduced to tube A after the 0 time point.

Long time points: Once a time point was reached, 100 μl was pipetted from tube A into 100 μl of 2 M NaCl (tube B, hypertonic solution to suspend small-molecule leakage). Ten microliters from tube B was diluted into 990 μl of a 1 M NaCl solution (tube C). Plating was performed immediately on Mueller Hinton agar supplemented with meropenem (8 mg/liter), preferably ending in 3 min. Tenfold dilutions were used for plating as follows: 100 μl from tube B → plate 1, 10 μl from tube B → plate 2, 100 μl from tube B → plate 2, 100 μl from tube C → plate 3, 10 μl from tube C → plate 4, 1 μl from tube C → plate 5.

Short time points: For all time points, 100 μl was pipetted from tube A into 100 μl of 2 M NaCl in 50% glycerol (tube B′, hypertonic solution to suspend small-molecule leakage, glycerol as a cryoprotectant). This tube was immediately flash-frozen in liquid nitrogen and stored at −80°C to completely stop AMP action. Further dilutions were performed for only after all time points were flash-frozen and safely stored. For each time point, tube B′ was thawed and 10 μl was immediately diluted in 990 μl of 1 M NaCl solution (tube C′). Plating was performed immediately, using the same protocol described previously for long time points. All the steps described here have also been illustrated in fig. S15.

$^{32}PO_4^{3-}$ leakage radioassay

A $^{32}PO_4^{3-}$ leakage radioassay was performed for Ω76 (32 mg/liter), colistin (5 mg/liter), and an untreated control against *A. baumannii* (P1270). Phosphate was used as a model small molecule to track the leakage of other essential small molecules during membrane disruption. As this protocol is complex, it has been illustrated in fig. S16.

Bloodstream absorption and elimination pharmacokinetics for N-terminal selenomethionine-labeled Ω76

For pharmacokinetic experiments, an N-terminal selenomethionine probe was attached to Ω76. The peptide's MBC against *A. baumannii* (table S5) remained unaffected by this alteration.

Six- to 8-week-old BALB/c mice (20 g weight) were used for these experiments. Mice were anesthetized with 2 mg of ketamine/0.16 mg of xylazine suspended in 200 μl of saline and injected intraperitoneally. Three types of samples were collected: (i) Cardiac punctures on anesthetized but untreated mice were first performed to assay baseline serum selenium content. (ii) Calibration controls were created by mixing known quantities of Nselmet-Ω76 into untreated mouse blood extracted via cardiac puncture. (iii) Later, mice were injected with Nselmet-Ω76 (70 mg/kg; corresponding to an Ω76 dose of 64 mg/kg), and cardiac punctures were performed at chosen time points in a 0- to 10-min range. It should be noted that, because of the difficulty involved in locating the mouse heart, time points could not be evenly sampled. Once blood was drawn from the heart, the time point for that sample was taken to be the mean time between the start and end of blood collection.

All blood samples were collected in clotting Vacutainer tubes (yellow top). After allowing the blood to clot for 1 hour, the serum from all blood samples was extracted by centrifuging at 6000 rpm/20 min and weighed out. Typically, 200 to 800 μl of blood were obtained from each mouse, which corresponded to 100 to 400 μl of serum. The mass for each sample was made up to 500 mg by diluting in high-performance liquid chromatography (HPLC)–grade DW. All samples were sent to Ramaiah Advanced Testing Lab (Bangalore) for quantification of selenium via ICP-MS. The serum concentration of Nselmet-Ω76 was then back-calculated from elemental selenium concentrations.

SEM experiments

A 10-ml bacterial culture inoculated in Mueller Hinton broth was incubated for 24 hours at 37°C at 180 rpm. This culture was centrifuged at

6000 rpm for 10 min. The pellet was resuspended in 0.8% saline, and the OD_{600} (optical density at 600 nm) of this culture was adjusted to 0.3 to 0.4. One microliter of test and control aliquots was then prepared. The test aliquot was treated with Ω76 (128 mg/liter). Both test and control aliquots were incubated at 37°C for 2 hours at 180 rpm. These aliquots were then centrifuged at 6000 rpm for 10 min and resuspended in a minimal volume of saline. Both aliquots were pipetted onto clean glass coverslips and allowed to air-dry and then fixed in 2.5% glutaraldehyde in saline for 24 hours. These samples were then washed thrice with water and dehydrated on an ethanol gradient (30, 50, 75, 85, 95, and 100%, 3 min each). Samples were dried at 65°C for 4 hours. Samples were attached to aluminum stubs, and a 10-nm gold coating was applied using an A Quorum Q150R ES sputter coater. The Carl Zeiss Ultra 55 field emission scanning electron microscope was used to acquire all SEM images. Samples were visualized under ×50,000 magnification using an SE2 probe with an extra-high tension voltage of 5 kV.

Preparation of bacterial protoplasts

β-Lactam–sensitive *A. baumannii* (B4505) protoplasts were prepared using a standard protocol (*63*). Briefly, *A. baumannii* was inoculated into 10 ml of Mueller Hinton broth and incubated overnight at 37°C/180 rpm (culture A). This culture (3 ml) was then inoculated into 10 ml of Mueller Hinton broth supplemented with 5% sucrose, 0.1% $MgSO_4$, and benzylpenicillin (100 mg/liter; penicillin G). This culture was incubated at 37°C for 2 hours at 180 rpm (culture B). Protoplasts were immediately used for SEM experiments. For AMP-treated and control groups, protoplasts were maintained in 0.8% saline supplemented with 5% sucrose, 0.1% $MgSO_4$, and benzylpenicillin (100 mg/liter; penicillin G).

Confocal microscopy experiments

Subcellular location experiments for Ω76 were performed using fluorescence confocal microscopy. Ω76 was linked to N-terminal FITC. Nile red and DAPI were used to counterstain the cell membrane and bacterial chromosome, respectively. Stock solutions of Nile red (2000 mg/liter in acetone), DAPI (1000 mg/liter in 5% 1,4-diazabicyclo[2.2.2]octane, 50% glycerol buffer), and FITC-labeled peptide (2000 mg/liter aqueous solution) were prepared. Cultures were inoculated in 10 ml of Mueller Hinton broth and incubated at 37°C for 12 hours at 180 rpm. A fivefold dilution in saline was performed (final volume, 1 ml), and the culture was pelleted down (6000 rpm for 10 min) and resuspended in 1 ml saline. One microliter of Nile red, 1 μl of DAPI, and 4 μl of FITC-labeled peptide stock solutions were added to this culture. A minimal quantity (5 μl) of culture was pipetted onto a clean glass slide and sealed with a clean glass coverslip. This slide was visualized using a Zeiss Observer Z.1 inverted fluorescence microscope under a 63× oil immersion objective. Individual stains were recorded using DAPI, GFP (green fluorescent protein), and DSRed2 filters and captured using the AxioVision Release 4.8.2 SP2 (08-2013) software. All images were captured <10 min after the introduction of fluorescent stains.

All images were saved as .png files. For clarity, 100 pixel–by–100 pixel representative regions were digitally magnified to 300 pixel × 300 pixel. All original images are provided in dataset S2. Quantification of stain colocalization was performed in two steps using a standard protocol (*43*). First, pixels were partitioned into two clusters using *K*-means clustering. The cluster with the lower mean was ignored, as it was considered to consist of background pixels. The cluster with the higher mean was taken forward, and Pearson's correlation was used to compare pixel intensity values. R/G (Nile red/FITC peptide), G/B (FITC peptide/DAPI), and R/B (Nile red/DAPI) channel correlations were calculated in this manner. Better stain colocalization was indicated by a higher Pearson's correlation and vice versa. Dataset S2 also contains Python scripts for image analysis and correlation calculation.

Preparation of samples for microarray analysis

Differential gene expression experiments were performed on a carbapenem- and tigecycline-resistant clinical *A. baumannii* isolate (P1270). This isolate was exposed to 0.1×, 0.25×, and 0.5× MIC concentrations of Ω76. A control cohort containing untreated *A. baumannii* (P1270) was also used. All samples were incubated at 37°C for 12 hours in 10 ml of Mueller Hinton broth supplemented with meropenem (8 mg/liter) to maintain the resistant phenotype. After incubation, these four samples were pelleted down at 6000 rpm for 10 min and flash-frozen with liquid N_2. Genotypic (India) performed quality control, RNA extraction, and *A. baumannii* microarray mRNA hybridization experiments using an Agilent CGH platform (Agilent *A. baumannii*_8X15k_GXP AMADID: 7936). Two technical replicates were performed for every sample, resulting in eight total samples.

Functional gene set enrichment analysis

We used the limma package included in Bioconductor (www.bioconductor.org/) in the R programming environment (http://cran.r-project.org/) for microarray data preprocessing. The read.images() function was used for median signal and background intensity extraction. The normexp() function (*64*) was used to background-adjust signal intensities. Quantile normalization and $\log_2$ transformation of these background-adjusted signals were then performed to ensure that signal intensities were consistent across each array (*64*). After preprocessing, information from the microarray custom dictionary file (CDF) was used to map probes to their corresponding genes.

Differential analysis was performed by comparing the gene expression levels of *A. baumannii* treated with 0.1×, 0.25×, and 0.5× MBC concentrations of Ω76 to those of the untreated *A. baumannii* control (GEO accession number: GSE116245). Genes with at least a 1.5 (2^0.584)–fold change (up- or down-regulation) and with a false discovery rate (FDR)–corrected *P* value of ≤0.05 calculated using the Benjamini and Hochberg method (*65*) were considered as significantly DEGs. This analysis revealed significant deregulation of 1835 (up-regulated, 951; down-regulated, 844), 1746 (up-regulated, 899; down-regulated, 847), and 840 (up-regulated, 431; down-regulated, 409) genes for 0.1×, 0.25×, and 0.5× MBC concentrations, respectively, in comparison to the untreated control.

Overlap analysis of these gene sets revealed that 279 genes (overlap-up) displayed at least a 1.5 (2^0.584)–fold up-regulation under all Ω76 concentrations tested (0.1×, 0.25×, and 0.5× MBC). Similarly, 333 genes (overlap-down) displayed at least a 1.5 (2^0.584)–fold down-regulation under all Ω76 concentrations tested (0.1×, 0.25×, and 0.5× MBC).

For enrichment analysis, we downloaded gene→GO term mappings from QuickGO (*66*) (dataset S4). GO terms attempt to classify genes under biologically relevant classes. For example, gene nuoN (NADH dehydrogenase) is classified under GO:0016020 (membrane), GO:0055114 (oxidation reduction process), and GO:0008137 (NADH dehydrogenase activity). Once every gene was assigned multiple corresponding GO terms, it was possible to determine which GO terms were significantly overrepresented or underrepresented in our data (overlap-up and overlap-down gene sets). For significance testing, we used two-sided hypergeometric distribution tests, with an FDR-corrected *P* value of ≤0.05 using Bonferroni adjustment. One hundred thirty-four

genes (GO-up) had significantly overrepresented GO terms in the overlap-up gene set. Similarly, 62 genes had significantly overrepresented GO terms in the overlap-down gene set (GO-down). Some genes may have incomplete GO assignments. Therefore, we checked the validity of all GO terms for all GO-up/GO-down genes. On the basis of a literature survey, we have included additional annotations for genes with incomplete GO assignments.

NMR spectroscopic experiments

Ω76 synthesized by GenScript was further purified by reversed-phase HPLC using a Varian Pursuit XRs 5 C18 semi-preparatory column (bead size, 5 μm; pore size, 100 Å) connected to a Waters 1525 binary HPLC pump with a Waters 2489 dual wavelength ultraviolet-visible detector. A linear gradient of Milli-Q water and acetonitrile (HPLC grade, Merck), both with added 0.1% trifluoroacetic acid (Spectrochem), was used. The fraction containing Ω76 was subsequently concentrated by rotary evaporation and lyophilized to dryness. Samples were prepared for NMR experiments by dissolving lyophilized Ω76 in either 100% CD_3OH (Sigma-Aldrich) or sterile Milli-Q water (10% D_2O, Cambridge Isotope Laboratories) containing 25 mM dodecylphosphocholine-d_{38} (Isotec). A peptide concentration of 1 mM was used in all NMR experiments.

Data were acquired on a 600-MHz Agilent NMR spectrophotometer fitted with a triple resonance cryogenically cooled probe with a single (*z* axis) pulsed-field gradient accessory. Homonuclear 2D experiments—^{1}H,^{1}H-TOCSY (mixing time, 65 ms) and ^{1}H,^{1}H-NOESY (mixing time, 150 ms)—were acquired on both samples. All NMR data were processed and analyzed on an Apple Macintosh system running OS X 10.10. The spectra were processed and visualized using NMRPipe 9.6 (*67*), and further assignment and analysis was carried out using CcpNmr Analysis 2.4 (*68*).

Distance restraints were extracted from the intensities of the assigned peaks in the ^{1}H,^{1}H-NOESY spectra using the "Make Distance Restraints" tool in CcpNmr Analysis. The maximum upper distance limit used was 6.0 Å, and all lower distance restraints for proton-proton pairs were set to 1.8 Å. Secondary chemical shifts and characteristic sequential NOEs were used to assign secondary structure, and backbone dihedral restraints and backbone hydrogen bond restraints were set accordingly. CYANA 3.0 (*69*) was used to calculate 400 structures after 20,000 steps of simulated annealing in torsion angle space, and the 50 structures with the lowest target function were evaluated using the MolProbity (*70*) server. The first 30 structures with a clashscore of 0 were chosen for the final ensemble structure.

The structure ensemble was evaluated using the online PSVS (*71*) server. Root-mean-square deviation (RMSD) calculations were carried out in MOLMOL 1.0 (*72*). Further analyses were carried out on the first model. The electrostatic surface was calculated using the ABPS tool in UCSF (University of California, San Francisco) Chimera (*73*). The 3D-HM vector (*61*) was calculated using the online tool at www.ibg.kit.edu/HM/. The 3D-HM vector and electrostatic surface potential were calculated assuming a solvent dielectric constant of 20.00 for the micelle-water interface, as an interpolation between the polar solvent exterior and the nonpolar micelle interior.

SUPPLEMENTARY MATERIALS

Supplementary material for this article is available at http://advances.sciencemag.org/cgi/content/full/5/7/eaax1946/DC1

Fig. S1. The origins of common subgraphical motifs shared by five Ω-family AMPs.
Fig. S2. Checkerboard assay to determine whether Ω76 and colistin in combination display a synergistic, additive, or antagonistic effect in vitro.
Fig. S3. Blood tests performed for multidose Ω76-treated mice in comparison to untreated control mice.
Fig. S4. Pilot experiments to determine the in vivo efficacy of Ω76 against *A. baumannii* (P1270) using a BALB/c mouse peritoneal model of infection.
Fig. S5. Independent replication experiment to confirm Ω76 activity against *A. baumannii* (P1270) in BALB/c mice, performed by A.D.
Fig. S6. SEM experiments performed for *A. baumannii* (B4505).
Fig. S7. SEM experiments performed for *A. baumannii* (B4505) protoplasts.
Fig. S8. SEM experiments performed for *E. coli* (K12 MG1655).
Fig. S9. SEM experiments performed for *S. flexneri* (MTCC1457).
Fig. S10. The classification of genes into GO terms after enrichment analysis.
Fig. S11. Ramachandran plot analysis of the best 30 structures of Ω76.
Fig. S12. The electrostatic surface potential and hydrophobic moment of Ω76.
Fig. S13. An illustration for all the steps required to determine the hemolytic activity of an AMP using human blood.
Fig. S14. Titration to determine the dose of *A. baumannii* (P1270) to be used for later efficacy experiments.
Fig. S15. The protocols used for generating time-kill curves are illustrated in detail.
Fig. S16. The protocol used for the $^{32}PO_4^{3-}$ leakage radioassay is illustrated in detail.
Table S1. A detailed tabulation depicting the origin of common subgraphical motifs shared by five Ω-family AMPs.
Table S2. MIC values expressed in micrograms per liter for 30 cultures tested against five designed peptides.
Table S3. MBC values expressed in micrograms per liter for Gram-positive cultures tested against two designed peptides displaying the highest I_scores (Ω17 and Ω76).
Table S4. MBC values expressed in micrograms per liter for Gram-negative cultures tested against two designed peptides displaying the highest I_scores (Ω17 and Ω76).
Table S5. MBC values expressed in micrograms per liter for seven clinical isolates of *A. baumannii*.
Table S6. 16*S* rRNA gene sequencing data for *A. baumannii* (P1270), confirming the genus and species.
Table S7. List of significantly up-regulated genes for *A. baumannii* (P1270) exposed to 0.1×, 0.25×, and 0.5× MBC concentrations of Ω76.
Table S8. List of significantly down-regulated genes for *A. baumannii* (P1270) exposed to 0.1×, 0.25×, and 0.5× MBC concentrations of Ω76.
Table S9. NMR restraints and structure evaluation statistics for Ω76 (30 structures).
Text S1. Coordinates of the 30 lowest-scoring NMR models of Ω76.
Dataset S1. Raw data for all figures.
Dataset S2. All original images acquired during confocal microscopy experiments are provided.
Dataset S3. Raw NOESY and TOCSY spectra.
Dataset S4. *A. baumannii* gene to GO term mappings.
Protocol S1. HELIGRAPHER.

REFERENCES AND NOTES

1. C. Fleischmann, A. Scherag, N. K. J. Adhikari, C. S. Hartog, T. Tsaganos, P. Schlattmann, D. C. Angus, K. Reinhart, International Forum of Acute Care Trialists, Assessment of global incidence and mortality of hospital-treated sepsis. Current estimates and limitations. *Am. J. Respir. Crit. Care Med.* **193**, 259–272 (2016).
2. J. O'Neill, Antimicrobial resistance: Tackling a crisis for the health and wealth of nations. *Rev. Antimicrob. Resist.* **1.1**, 1–16 (2014).
3. J.-L. Vincent, J. C. Marshall, S. A. Ñamendys-Silva, B. François, I. Martin-Loeches, J. Lipman, K. Reinhart, M. Antonelli, P. Pickkers, H. Njimi, E. Jimenez, Y. Sakr, ICON investigators, Assessment of the worldwide burden of critical illness: The intensive care over nations (ICON) audit. *Lancet Respir. Med.* **2**, 380–386 (2014).
4. H. Erbay, A. N. Yalcin, S. Serin, H. Turgut, E. Tomatir, B. Cetin, M. Zencir, Nosocomial infections in intensive care unit in a turkish university hospital: A 2-year survey. *Intensive Care Med.* **29**, 1482–1488 (2003).
5. N. Y. A. Aly, H. H. Al-Mousa, M. El Sayed, Nosocomial infections in a medical-surgical intensive care unit. *Med. Princ. Pract.* **17**, 373–377 (2008).
6. M. J. Neidell, B. Cohen, Y. Furuya, J. Hill, C. Y. Jeon, S. Glied, E. L. Larson, Costs of healthcare-and community-associated infections with antimicrobial-resistant versus antimicrobial-susceptible organisms. *Clin. Infect. Dis.* **55**, 807–815 (2012).
7. A. Y. Peleg, H. Seifert, D. L. Paterson, *Acinetobacter baumannii*: Emergence of a successful pathogen. *Clin. Microbiol. Rev.* **21**, 538–582 (2008).
8. World Health Organization, *Global Priority List of Antibiotic-Resistant Bacteria to Guide Research, Discovery, and Development of New Antibiotics* (World Health Organization, 2017).
9. K. M. Papp-Wallace, A. Endimiani, M. A. Taracila, R. A. Bonomo, Carbapenems: Past, present, and future. *Antimicrob. Agents Chemother.* **55**, 4943–4960 (2011).
10. C.-H. Su, J.-T. Wang, C. A. Hsiung, L.-J. Chien, C.-L. Chi, H.-T. Yu, F.-Y. Chang, S.-C. Chang, Increase of carbapenem-resistant *Acinetobacter baumannii* infection in acute care

hospitals in Taiwan: Association with hospital antimicrobial usage. *PLOS ONE* **7**, e37788 (2012).
11. E. Garza-González, J. M. Llaca-Díaz, F. J. Bosques-Padilla, G. M. González, Prevalence of multidrug-resistant bacteria at a tertiary-care teaching hospital in Mexico: Special focus on Acinetobacter baumannii. *Chemotherapy* **56**, 275–279 (2010).
12. L. Poirel, P. Nordmann, Carbapenem resistance in *Acinetobacter baumannii*: Mechanisms and epidemiology. *Clin. Microbiol. Infect.* **12**, 826–836 (2006).
13. W.-H. Sheng, J.-T. Wang, S.-Y. Li, Y.-C. Lin, A. Cheng, Y.-C. Chen, S.-C. Chang, Comparative in vitro antimicrobial susceptibilities and synergistic activities of antimicrobial combinations against carbapenem-resistant acinetobacter species: *Acinetobacter baumannii* versus *Acinetobacter* genospecies 3 and 13TU. *Diagn. Microbiol. Infect. Dis.* **70**, 380–386 (2011).
14. S. Navon-Venezia, A. Leavitt, Y. Carmeli, High tigecycline resistance in multidrug-resistant *Acinetobacter baumannii*. *J. Antimicrob. Chemother.* **59**, 772–774 (2007).
15. M. Deng, M.-H. Zhu, J.-J. Li, S. Bi, Z.-K. Sheng, F.-S. Hu, J.-J. Zhang, W. Chen, X.-W. Xue, J.-F. Sheng, L.-J. Li, Molecular epidemiology and mechanisms of tigecycline resistance in clinical isolates of *Acinetobacter baumannii* from a chinese university hospital. *Antimicrob. Agents Chemother.* **58**, 297–303 (2013).
16. I. I. Balkan, M. Dogan, B. Durdu, A. Batirel, I. N. Hakyemez, B. Cetin, O. Karabay, I. Gonen, A. S. Ozkan, S. Uzun, M. E. Demirkol, S. Akbas, A. B. Kacmaz, S. Aras, A. Mert, F. Tabak, Colistin nephrotoxicity increases with age. *Scand. J. Infect. Dis.* **46**, 678–685 (2014).
17. H. J. Ko, M. H. Jeon, E. J. Choo, E. J. Lee, T. H. Kim, J. B. Jun, H. W. Gil, Early acute kidney injury is a risk factor that predicts mortality in patients treated with colistin. *Nephron Clin. Pract.* **117**, c284–c288 (2011).
18. J. D. Hartzell, R. Neff, J. Ake, R. Howard, S. Olson, K. Paolino, M. Vishnepolsky, A. Weintrob, G. Wortmann, Nephrotoxicity associated with intravenous colistin (colistimethate sodium) treatment at a tertiary care medical center. *Clin. Infect. Dis.* **48**, 1724–1728 (2009).
19. A. Peschel, H.-G. Sahl, The co-evolution of host cationic antimicrobial peptides and microbial resistance. *Nat. Rev. Microbiol.* **4**, 529–536 (2006).
20. K. Matsuzaki, O. Murase, N. Fujii, K. Miyajima, An antimicrobial peptide, magainin 2, induced rapid flip-flop of phospholipids coupled with pore formation and peptide translocation. *Biochemistry* **35**, 11361–11368 (1996).
21. G. Baumann, P. Mueller, A molecular model of membrane excitability. *J. Supramol. Struct.* **2**, 538–557 (1974).
22. Y. Shai, Mode of action of membrane active antimicrobial peptides. *Biopolymers* **66**, 236–248 (2002).
23. K. A. Brogden, Antimicrobial peptides: Pore formers or metabolic inhibitors in bacteria? *Nat. Rev. Microbiol.* **3**, 238–250 (2005).
24. H. Gusman, J. Travis, E. J. Helmerhorst, J. Potempa, R. F. Troxler, F. G. Oppenheim, Salivary histatin 5 is an inhibitor of both host and bacterial enzymes implicated in periodontal disease. *Infect. Immun.* **69**, 1402–1408 (2001).
25. A. Yonezawa, J. Kuwahara, N. Fujii, Y. Sugiura, Binding of tachyplesin I to DNA revealed by footprinting analysis: Significant contribution of secondary structure to dna binding and implication for biological action. *Biochemistry* **31**, 2998–3004 (2002).
26. C. Subbalakshmi, N. Sitaram, Mechanism of antimicrobial action of indolicidin. *FEMS Microbiol. Lett.* **160**, 91–96 (1998).
27. A. Patrzykat, C. L. Friedrich, L. Zhang, V. Mendoza, R. E. W. Hancock, Sublethal concentrations of pleurocidin-derived antimicrobial peptides inhibit macromolecular synthesis in *Escherichia coli*. *Antimicrob. Agents Chemother.* **46**, 605–614 (2002).
28. M. Mardirossian, R. Grzela, C. Giglione, T. Meinnel, R. Gennaro, P. Mergaert, M. Scocchi, The host antimicrobial peptide bac7$_{1\text{-}35}$ binds to bacterial ribosomal proteins and inhibits protein synthesis. *Chem. Biol.* **21**, 1639–1647 (2014).
29. T. Florin, C. Maracci, M. Graf, P. Karki, D. Klepacki, O. Berninghausen, R. Beckmann, N. Vázquez-Laslop, D. N. Wilson, M. V. Rodnina, A. S. Mankin, An antimicrobial peptide that inhibits translation by trapping release factors on the ribosome. *Nat. Struct. Mol. Biol.* **24**, 752–757 (2017).
30. C. L. Friedrich, D. Moyles, T. J. Beveridge, R. E. W. Hancock, Antibacterial action of structurally diverse cationic peptides on gram-positive bacteria. *Antimicrob. Agents Chemother.* **44**, 2086–2092 (2000).
31. P. Sass, A. Jansen, C. Szekat, V. Sass, H.-G. Sahl, G. Bierbaum, The lantibiotic mersacidin is a strong inducer of the cell wall stress response of *Staphylococcus aureus*. *BMC Microbiol.* **8**, 186 (2008).
32. J. L. Fox, Antimicrobial peptides stage a comeback. *Nat. Biotechnol.* **31**, 379–382 (2013).
33. M. Wenzel, A. I. Chiriac, A. Otto, D. Zweytick, C. May, C. Schumacher, R. Gust, H. B. Albada, M. Penkova, U. Krämer, R. Erdmann, N. Metzler-Nolte, S. K. Straus, E. Bremer, D. Becher, H. Brötz-Oesterhelt, H.-G. Sahl, J. E. Bandow, Small cationic antimicrobial peptides delocalize peripheral membrane proteins. *Proc. Natl. Acad. Sci. U.S.A.* **111**, E1409–E1418 (2014).
34. Y. Ge, D. L. MacDonald, K. J. Holroyd, C. Thornsberry, H. Wexler, M. Zasloff, In vitro antibacterial properties of pexiganan, an analog of magainin. *Antimicrob. Agents Chemother.* **43**, 782–788 (1999).
35. A. de Breij, M. Riool, R. A. Cordfunke, N. Malanovic, L. de Boer, R. I. Koning, E. Ravensbergen, M. Franken, T. van der Heijde, B. K. Boekema, P. H. S. Kwakman, N. Kamp, A. el Ghalbzouri, K. Lohner, S. A. J. Zaat, J. W. Drijfhout, P. H. Nibbering, The antimicrobial peptide Saap-148 combats drug-resistant bacteria and biofilms. *Sci. Transl. Med.* **10**, eaan4044 (2018).
36. B. Deslouches, J. D. Steckbeck, J. K. Craigo, Y. Doi, T. A. Mietzner, R. C. Montelaro, Rational design of engineered cationic antimicrobial peptides consisting exclusively of arginine and tryptophan, and their activity against multidrug-resistant pathogens. *Antimicrob. Agents Chemother.* **57**, 2511–2521 (2013).
37. S. E. Blondelle, R. A. Houghten, Design of model amphipathic peptides having potent antimicrobial activities. *Biochemistry* **31**, 12688–12694 (2002).
38. Y. Huang, N. Wiradharma, K. Xu, Z. Ji, S. Bi, L. Li, Y.-Y. Yang, W. Fan, Cationic amphiphilic alpha-helical peptides for the treatment of carbapenem-resistant *Acinetobacter baumannii* infection. *Biomaterials* **33**, 8841–8847 (2012).
39. B. Deslouches, S. M. Phadke, V. Lazarevic, M. Cascio, K. Islam, R. C. Montelaro, T. A. Mietzner, De novo generation of cationic antimicrobial peptides: Influence of length and tryptophan substitution on antimicrobial activity. *Antimicrob. Agents Chemother.* **49**, 316–322 (2004).
40. S. J. Lam, N. M. O'Brien-Simpson, N. Pantarat, A. Sulistio, E. H. H. Wong, Y.-Y. Chen, J. C. Lenzo, J. A. Holden, A. Blencowe, E. C. Reynolds, G. G. Qiao, Combating multidrug-resistant gram-negative bacteria with structurally nanoengineered antimicrobial peptide polymers. *Nat. Microbiol.* **1**, 16162 (2016).
41. G. Maccari, M. di Luca, R. Nifosí, F. Cardarelli, G. Signore, C. Boccardi, A. Bifone, Antimicrobial peptides design by evolutionary multiobjective optimization. *PLOS Comput. Biol.* **9**, e1003212 (2013).
42. C. Loose, K. Jensen, I. Rigoutsos, G. Stephanopoulos, A linguistic model for the rational design of antimicrobial peptides. *Nature* **443**, 867–869 (2006).
43. D. Nagarajan, T. Nagarajan, N. Roy, O. Kulkarni, S. Ravichandran, M. Mishra, D. Chakravortty, N. Chandra, Computational antimicrobial peptide design and evaluation against multidrug-resistant clinical isolates of bacteria. *J. Biol. Chem.* **293**, 3492–3509 (2018).
44. C. D. Fjell, H. Jenssen, W. A. Cheung, R. E. W. Hancock, A. Cherkasov, Optimization of antibacterial peptides by genetic algorithms and cheminformatics. *Chem. Biol. Drug Des.* **77**, 48–56 (2011).
45. W. F. Porto, L. Irazazabal, E. S. F. Alves, S. M. Ribeiro, C. O. Matos, Á. S. Pires, I. C. M. Fensterseifer, V. J. Miranda, E. F. Haney, V. Humblot, M. D. T. Torres, R. E. W. Hancock, L. M. Liao, A. Ladram, T. K. Lu, C. de la Fuente-Nunez, O. L. Franco, In silico optimization of a guava antimicrobial peptide enables combinatorial exploration for peptide design. *Nat. Commun.* **9**, 1490 (2018).
46. T. Katsu, C. Ninomiya, M. Kuroko, H. Kobayashi, T. Hirota, Y. Fujita, Action mechanism of amphipathic peptides gramicidin S and melittin on erythrocyte membrane. *Biochim. Biophys. Acta* **939**, 57–63 (1988).
47. C. E. Dempsey, The actions of melittin on membranes. *Biochim. Biophys. Acta* **1031**, 143–161 (1990).
48. M. I. A. van der Kraan, J. Groenink, K. Nazmi, E. C. Veerman, J. G. M. Bolscher, A. V. Nieuw Amerongen, Lactoferrampin: A novel antimicrobial peptide in the n1-domain of bovine lactoferrin. *Peptides* **25**, 177–183 (2004).
49. Z. Wang, G. Wang, APD: The Antimicrobial Peptide Database. *Nucleic Acids Res.* **32**, D590–D592 (2004).
50. B. Kuhlman, G. Dantas, G. C. Ireton, G. Varani, B. L. Stoddard, D. Baker, Design of a novel globular protein fold with atomic-level accuracy. *Science* **302**, 1364–1368 (2018).
51. D. Nagarajan, S. Sukumaran, G. Deka, K. Krishnamurthy, H. S. Atreya, N. Chandra, Design of a heme-binding peptide motif adopting a β-hairpin conformation. *J. Biol. Chem.* (2018).
52. D. Nagarajan, G. Deka, M. Rao, Design of symmetric tim barrel proteins from first principles. *BMC Biochem.* **16**, 18 (2015).
53. M. D. Johnson, C. MacDougall, L. Ostrosky-Zeichner, J. R. Perfect, J. H. Rex, Combination antifungal therapy. *Antimicrob. Agents Chemother.* **48**, 693–715 (2004).
54. FDA guidelines for meropenem usage; www.accessdata.fda.gov/drugsatfda_docs/label/2014/050706s035lbl.pdf [accessed 2 June 2018].
55. FDA guidelines for tigecycline usage; www.accessdata.fda.gov/drugsatfda_docs/label/2013/021821s026s031lbl.pdf [accessed 2 June 2018].
56. S. Biswas, J.-M. Brunel, J.-C. Dubus, M. Reynaud-Gaubert, J.-M. Rolain, Colistin: An update on the antibiotic of the 21st century. *Expert. Rev. Anti Infect. Ther.* **10**, 917–934 (2014).
57. W. Hengzhuang, H. Wu, O. Ciofu, Z. Song, N. Høiby, In vivo pharmacokinetics/pharmacodynamics of colistin and imipenem in *Pseudomonas aeruginosa* on biofilm. *Antimicrob. Agents Chemother.* **56**, 2683–2690 (2012).
58. F. Thalhammer, P. Schenk, H. Burgmann, I. el Menyawi, U. M. Hollenstein, A. R. Rosenkranz, G. Sunder-Plassmann, S. Breyer, K. Ratheiser, Single-dose pharmacokinetics of meropenem during continuous venovenous hemofiltration. *Antimicrob. Agents Chemother.* **42**, 2417–2420 (1998).

59. R. White, L. Friedrich, D. Burgess, D. Warkentin, J. Bosso, Comparative in vitro pharmacodynamics of imipenem and meropenem against Pseudomonas aeruginosa. *Antimicrob. Agents Chemother.* **40**, 904–908 (1996).
60. Z. Jiang, A. I. Vasil, J. D. Hale, R. E. W. Hancock, M. L. Vasil, R. S. Hodges, Effects of net charge and the number of positively charged residues on the biological activity of amphipathic α-helical cationic antimicrobial peptides. *Biopolymers* **90**, 369–383 (2008).
61. S. Reißer, E. Strandberg, T. Steinbrecher, A. S. Ulrich, 3D hydrophobic moment vectors as a tool to characterize the surface polarity of amphiphilic peptides. *Biophys. J.* **106**, 2385–2394 (2014).
62. I. Wiegand, K. Hilpert, R. E. W. Hancock, Agar and broth dilution methods to determine the minimal inhibitory concentration (MIC) of antimicrobial substances. *Nat. Protoc.* **3**, 163–175 (2008).
63. J. Lederberg, Bacterial protoplasts induced by penicillin. *Proc. Natl. Acad. Sci. U.S.A.* **42**, 574–577 (1956).
64. G. Smyth, limma: Linear models for microarray data, in *Bioinformatics and Computational Biology Solutions Using R and Bioconductor. Statistics for Biology and Health*, R. Gentleman, V. J. Carey, W. Huber, R. A. Irizarry, S. Dudoit, Eds. (Springer, 2005).
65. Y. Benjamini, Y. Hochberg, Controlling the false discovery rate: A practical and powerful approach to multiple testing. *J. R. Stat. Soc. Ser. B* **57**, 289–300 (1995).
66. D. Binns, E. Dimmer, R. Huntley, D. Barrell, C. O'Donovan, R. Apweiler, Quickgo: A web-based tool for gene ontology searching. *Bioinformatics* **25**, 3045–3046 (2009).
67. F. Delaglio, S. Grzesie, G. W. Vuister, G. Zhu, J. Pfeifer, A. Bax, Nmrpipe: A multidimensional spectral processing system based on UNIX pipes. *J. Biomol. NMR* **6**, 277–293 (1995).
68. W. F. Vranken, W. Boucher, T. J. Stevens, R. H. Fogh, A. Pajon, M. Llinas, E. L. Ulrich, J. L. Markley, J. Ionides, E. D. Laue, The CCPN data model for NMR spectroscopy: Development of a software pipeline. *Proteins* **59**, 687–696 (2005).
69. P. Güntert, Structure calculation of biological macromolecules from nmr data. *Q. Rev. Biophys.* **31**, 145–237 (1998).
70. V. B. Chen, W. B. Arendall III, J. J. Headd, D. A. Keedy, R. M. Immormino, G. J. Kapral, L. W. Murray, J. S. Richardson, D. C. Richardson, MolProbity: All-atom structure validation for macromolecular crystallography. *Acta Crystallogr. D Biol. Crystallogr.* **66**, 12–21 (2010).
71. A. Bhattacharya, R. Tejero, G. T. Montelione, Evaluating protein structures determined by structural genomics consortia. *Proteins* **66**, 778–795 (2007).
72. R. Koradi, M. Billeter, K. Wüthrich, Molmol: A program for display and analysis of macromolecular structures. *J. Mol. Graph.* **14**, 51–55 (1996).
73. E. F. Pettersen, T. D. Goddard, C. C. Huang, G. S. Couch, D. M. Greenblatt, E. C. Meng, T. E. Ferrin, Ucsf chimera—A visualization system for exploratory research and analysis. *J. Comput. Chem.* **25**, 1605–1612 (2004).

Acknowledgments: We thank DBT and the Department of Science and Technology (DST; India) for the NMR and mass spectrometric facilities at the Indian Institute of Science. We thank Satya Tapas for contributing essential materials for this project. We thank P. Kar, who, during his summer internship, helped work on the Heligrapher design concept. The HeLa cell line was provided by A. Karande, and we thank her for the same. We thank the CAF (IISc) for providing large numbers of BALB/c mice used in this study. We thank the MNCF facility (CeNSE, IISc) for SEM access. **Funding:** We thank the Department of Biotechnology (DBT; India) for financial support to our laboratory. **Author contributions:** D.N. conceived the maximum common subgraph algorithm and implemented the Heligrapher software package (Fig. 1). D.N. designed, performed, and analyzed experiments (Figs. 2 to 4 and Table 2). D.N. prepared samples for microarray analysis and analyzed microarray data after processing (Fig. 6). N.R. performed all NMR experiments (Fig. 7, table S9, and figs. S11 and S12) under the supervision of S.P.S. O.K. co-performed experiments (Figs. 2, D, F, and G to L, and 3C). N.N. co-performed experiments (Fig. 5). A.D. performed the independent replication experiment to confirm our findings in Fig. 3 (fig. S5). S.R. processed all microarray data (Fig. 6 and fig. S10). C.T. co-performed experiments (Figs. 2E and 3, D and E). I.V.A. and S.T. compiled disc diffusion susceptibility data in tables S3 and S4. N.C. generated the idea and initiated the study. D.C. and N.C. coordinated the study, planned experiments, and provided resources. All authors reviewed the manuscript. **Competing interests:** All authors declare that they have no competing interests exist. **Data and materials availability:** All data needed to evaluate the conclusions in the paper are present in the paper and/or the Supplementary Materials. Additional data related to this paper may be requested from the authors.

Submitted 1 March 2019
Accepted 17 June 2019
Published 24 July 2019
10.1126/sciadv.aax1946

Citation: D. Nagarajan, N. Roy, O. Kulkarni, N. Nanajkar, A. Datey, S. Ravichandran, C. Thakur, S. T., I. V. Aprameya, S. P. Sarma, D. Chakravortty, N. Chandra, Ω76: A designed antimicrobial peptide to combat carbapenem- and tigecycline-resistant *Acinetobacter baumannii*. *Sci. Adv.* **5**, eaax1946 (2019).

ScienceAdvances

#76: A designed antimicrobial peptide to combat carbapenem- and tigecycline-resistant *Acinetobacter baumannii*

Deepesh Nagarajan, Natasha Roy, Omkar Kulkarni, Neha Nanajkar, Akshay Datey, Sathyabaarathi Ravichandran, Chandrani Thakur, Sandeep T., Indumathi V. Aprameya, Siddhartha P. Sarma, Dipshikha Chakravortty, and Nagasuma Chandra

Sci. Adv., **5** (7), eaax1946.
DOI: 10.1126/sciadv.aax1946